

Weyl Magnons in the Non-Coplanar Antiferromagnet MnTe₂

Ahmed E. Fahmy^{1,*,\dagger}, Archibald J. Williams^{2,*}, Yufei Li^{1,*,\dagger}, Thuc T. Mai³, Kevin F. Garrity⁴, Matthew B. Stone⁵, Mohammed J. Karaki¹, Sara Haravifard^{6,7}, Angela R. Hight Walker³, Rolando Valdés Aguilar^{1,\dagger}, Joshua E. Goldberger^{2,\dagger}, and Yuan-Ming Lu^{1,\dagger}

¹*Department of Physics, The Ohio State University, Columbus, OH 43210, USA*

²*Department of Chemistry and Biochemistry, The Ohio State University, Columbus, OH 43210, USA*

³*Quantum Measurements Division, Physical Measurement Laboratory, National Institute of Standards and Technology, Gaithersburg, MD 20899, USA*

⁴*Materials Measurement Science Division, Material Measurement Laboratory, National Institute of Standards and Technology, Gaithersburg, MD 20899, USA*

⁵*Neutron Scattering Division, Oak Ridge National Laboratory, Oak Ridge, Tennessee 37831, United States of America*

⁶*Department of Physics, Duke University, Durham, North Carolina 27708, USA*

⁷*Department of Mechanical Engineering and Materials Science, Duke University, Durham, North Carolina 27708, USA*

*These authors contributed equally to this work.

Using a combination of band representation analysis, inelastic neutron scattering (INS), magneto-Raman spectroscopy measurements, and linear spin wave theory, we establish that the non-coplanar antiferromagnet MnTe₂ is a tunable Weyl magnon material, hosting symmetry-protected topological nodal lines in its magnon band structure, protected by the non-coplanar nature of the antiferromagnetic ordering, that transition into Weyl magnons upon the application of symmetry-breaking perturbations using an external magnetic field. By constructing a spin model that reproduces the observed INS magnon spectra and field-dependence of the Raman Γ -magnons, we directly probe the topological magnon nodal lines and observe their associated signature of non-trivial topology through the pseudo-spin winding of the scattering intensity in angular scans near the nodal lines. Finally, we discuss how to induce Weyl magnons in the spectrum through an external magnetic field, shedding light on future in-field INS and thermal Hall experiments. This work establishes a clear magnonic analog to Weyl electrons, enabling further exploration of topological behavior in bosonic systems and highlighting the interplay between magnetic order and band topology in non-coplanar antiferromagnets.

Introduction

In magnetically ordered materials, low-energy spin excitations manifest as quantized collective modes known as magnons. These quasiparticles are the chargeless bosonic analogues of electrons in solids, can propagate through the lattice, and have well-defined energy bands in momentum space. When these magnon bands acquire non-trivial topological characteristics—such as Berry curvature, Chern number, or protected edge states—the resulting excitations are termed topological magnons^{1–3}. These excitations are protected by the underlying symmetries and topology of the magnetic structure, making them robust against elastic backscattering from defects or disorder^{4,5}. Owing to their bosonic statistics and intrinsic magnetic moment, magnons can transport angular momentum without electric charge, offering a potential platform for low-dissipation spin transport^{6,7}. The confluence of topological protection and spin-carrying capacity has spurred proposals for a variety of topological magnonic devices, including chiral spin-wave waveguides, thermal Hall-based logic elements, and unidirectional magnon diodes^{7–9}. In particular, Weyl magnons^{10–14} are a striking subclass of topological magnons in which isolated, linear band crossings (Weyl points) appear in 3D momentum space, acting as monopoles of Berry curvature and enforcing nonzero Chern numbers on intermediate 2D slices of the Brillouin zone (BZ). Therefore, their surface projections are joined by open magnon-arc modes^{12,15}, and the resulting Berry-curvature flux yields pronounced anomalous thermal Hall and chiral magnon transport features. A hallmark of these excitations is their tunability: Weyl nodes can be created, shifted, or annihilated by external perturbations such as magnetic fields or strain, offering an unusual degree of control over topological bosonic quasiparticles.

Quasiparticle Weyl excitations have been experimentally confirmed not only in electronic systems^{16,17}, but also in artificial photonic crystals¹⁸ and phononic crystals¹⁹. However, no clear evidence for Weyl magnons has been found despite several theoretically-proposed spin models that predict Weyl magnons^{10–14}. From a symmetry perspective, Weyl electrons^{20,21} are forbidden in the presence of a combined inversion \mathcal{I} and time-reversal \mathcal{T} symmetry that give rise to two-fold Kramers' degeneracy of bands. However, magnonic systems are fundamentally different; magnetic order breaks physical time reversal symmetry and magnons are integer spin, bosonic excitations that do not follow Kramers' theorem where $\mathcal{T}^2 = +1$. This suggests that Weyl magnons will generally be allowed in magnonic band structures. However, even in the absence of time reversal symmetry, coplanar Heisenberg magnets have an effective time reversal symmetry $\bar{\mathcal{T}}$, a product of time reversal and a global π -spin rotation, that can prohibit Weyl magnons when the system is inversion-symmetric²². This results from the constraints that each symmetry places on the Berry curvature $\Omega_n(\vec{k})$ of magnon bands: inversion imposes $\Omega_n(\vec{k}) = \Omega_n(-\vec{k})$ and effective time reversal imposes $\Omega_n(\vec{k}) = -\Omega_n(-\vec{k})$. Combined, they result in a vanishing Berry

^{\dagger} Corresponding authors: abdelazim.2@osu.edu & rvaldesag@gmail.com & goldberger.4@osu.edu & lu.1435@osu.edu

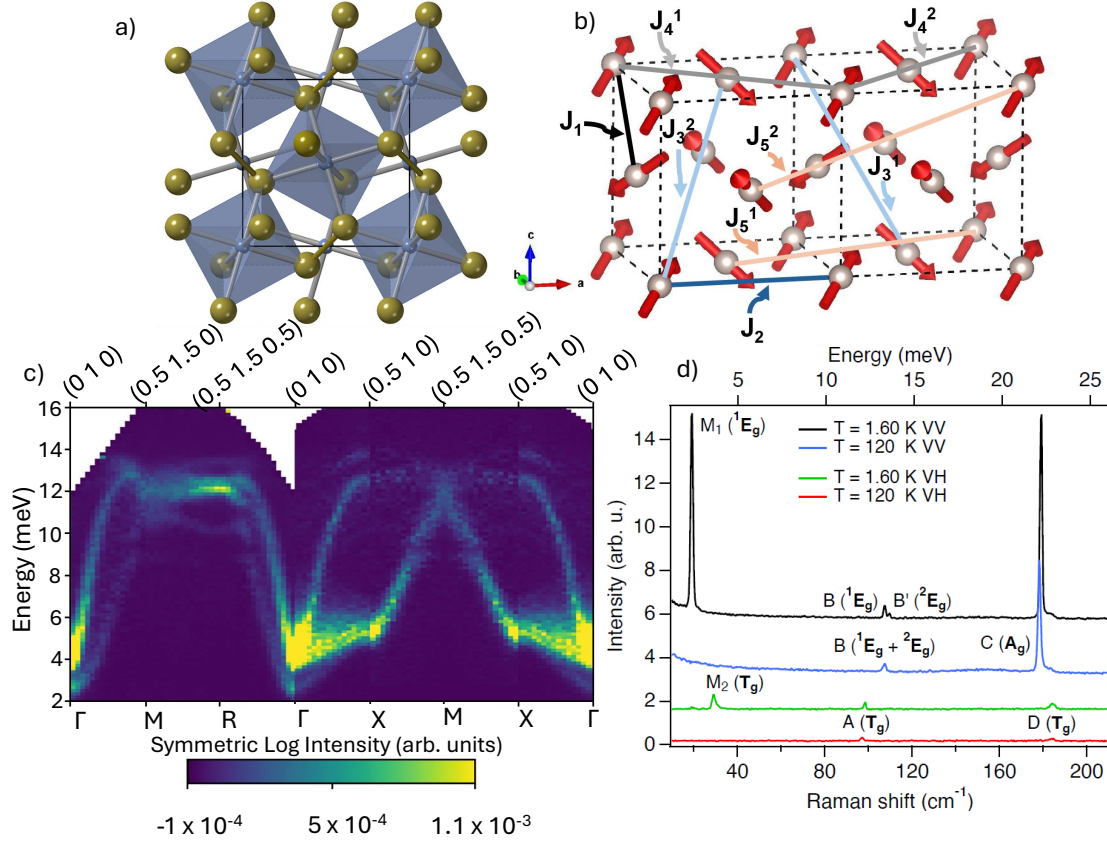


Figure 1: a) Crystal Structure of MnTe_2 : blue and gold spheres represent the Mn and Te ions, respectively. Each Mn ion is bonded to six Te ions forming tilted corner-sharing octahedra, colored in blue gray. b) The magnetic structure of MnTe_2 highlighting the different J couplings used for the LSWT fitting. The dotted lines indicate the magnetic unit cell and the coincident nuclear unit cell. c) Inelastic neutron scattering measurements of MnTe_2 at 5 K along the principal directions in reciprocal space, with the different directions merged together. d) Temperature dependent Raman spectra above and below T_N , collected in both parallel (VV) and cross (VH) polarization configurations. The two magnons are labeled M_1 and M_2 while the four phonons are labeled A-D in increasing energy, with symmetries noted in parentheses.

curvature. Since Weyl points are effectively monopole sources or sinks of Berry curvature, Weyl points are prohibited in the presence of both \mathcal{I} and $\bar{\mathcal{T}}$ symmetries. This serves as the key motivation for choosing a non-coplanar, magnetically-ordered material without an effective time-reversal symmetry in order to realize Weyl magnons.

While there have been previous reports on observations of topological magnons^{23–30}, these have mainly been confined to hexagonal lattices, with collinear magnetic orders often involving Dirac crossings at high-symmetry points, or magnon Chern insulators. These examples provide limited generalization across broader material classes and geometries, restricting progress in scalable magnonic engineering. To realize the potential of topological magnonics in applications, it is crucial to first develop a unified theoretical and algorithmic framework capable of identifying diverse topological features across a wide range of magnetic materials. This has been accomplished recently¹⁵ where it was shown how to use the symmetry of the magnetic structure and the atomic positions of the magnetic atoms to theoretically determine the topology of magnon bands. Here, we use those theoretical results and integrate them with experimental inelastic neutron scattering (INS), magneto-Raman scattering, and Hamiltonian modeling to prove the existence of topological magnon nodal lines. These gap out into tunable Weyl magnons when a magnetic field in a low-symmetry direction is applied. Direct evidence of these topological nodal lines in MnTe_2 are observed in zero-field INS through the angular dependence of the scattering intensity, revealing a characteristic pseudo-spin winding consistent with nontrivial magnon topology. These results establish MnTe_2 as a direct bosonic analogue of electronic Weyl systems, open new avenues for exploring topological excitations in non-coplanar magnetic insulators, and constitute a compelling experimental and theoretical demonstration of Weyl magnons.

Symmetry-Based Topology Indicators

Among the recently developed catalog of topological magnon materials in Ref¹⁵, MnTe_2 was selected as a suitable target material to experimentally confirm the presence of topological Weyl magnons. It is an ideal candidate to confirm the presence of topological magnon bands due to its air stability, accessible transition temperature ($T_N \sim 87$ K), and electronic insulating behavior (energy gap $E_g = 0.87$ eV). MnTe_2 was also selected for its simple chemical formulation and the ease of large single-crystal growth (see Supplementary Sections 1 & 2) appropriate for the measurement of topological magnons. MnTe_2 crystallizes into the cubic pyrite structure in space group $Pa\bar{3}$ as illustrated in Fig. 1 (a). The Mn atoms sit in corner sharing MnTe_6 octahedra and are further connected by Te_2^{2-} dimers. This results in Mn^{2+} ions with $S = 5/2$ on the atomic Wyckoff Position (WP) $4a$ with site symmetry group of $\bar{3}$, where the 3-fold axis points along the $[111]$ crystal direction. Below the Néel temperature, the Mn^{2+} moments order antiferromagnetically into a non-coplanar magnetic

structure shown in Fig. 1(b) which can be described as four sublattices of Mn atoms with each Mn sublattice having moments that point along different local [111] directions, resulting in no net magnetic moment in the unit cell.

Despite this magnetic ordering, the unit cell remains unchanged, resulting in a magnetic space group (MSG) of $Pa\bar{3}$. The magnon band representation induced from the WP 4a is:

$$({}^1E_g)_{4a} \uparrow Pa\bar{3}(205.33) = \Gamma_3^+(1) \oplus \Gamma_4^+(3) \oplus M_1(2) \oplus M_2(2) \oplus R_2^+(2) \oplus R_3^+(2) \oplus X_1(2) \oplus X_2(2) \quad (1)$$

where the MSG symmetries protect a three-fold degeneracy at the Brillouin zone center (Γ) of the Γ_4^+ magnon, and two doubly degenerate points at the X, M, R momenta of the Brillouin zone, as verified by the combination of the INS and magneto-Raman measurements shown in Fig. 2. This clearly demonstrates the compatibility relations of the magnon band *irreps* (i.e. how magnon bands decompose and merge on the different high-symmetry manifolds of the BZ) schematically represented in the upper panel of Fig. 3 (a). For example, on the line from Γ to R , the triply-degenerate Γ_4^+ magnon at Γ splits into three single bands and one of those combines with the singly-degenerate Γ_3^+ magnon to form a doubly degenerate magnon at R where the other two bands also combine to form the other doubly-degenerate magnon, giving rise to the pair of two-fold degeneracies at R . These two doubly-degenerate magnon bands remain unbroken along the high-symmetry lines $R - M$ and $M - X$. Along $X - \Gamma$, each doubly-degenerate mode split into two single bands, and one of the single bands of one doubly-degenerate magnon combine with the two single bands of the other doubly-degenerate magnon to form the triply-degenerate Γ magnon while the remaining band becomes the singly-degenerate Γ mode. Additionally, an investigation of the compatibility relations on the $k_i = 0$ high-symmetry planes reveals the existence of unavoidable nodal lines on these planes as demonstrated in the crossing between the $M(1/2, 1/2, 0)$ and $\{3_{111}^-|0\}k_X$ momenta shown in Fig. 3 (a) (see also Supplementary Section 4).

Weyl magnons, however, can be induced in the band structure of $MnTe_2$ upon the inclusion of certain symmetry-breaking perturbations as predicted through the symmetry-based algorithm¹⁵ as following. Out of the 10 subgroups of $Pa\bar{3}$ that can be realized by applying external perturbations¹², only 5 have nontrivial symmetry indicator (SI) groups³¹. Among those, only one subgroup, $P\bar{1}$, host type-I topological magnons (i.e. guaranteed perturbation-induced magnon topology)¹⁵. This subgroup can be realized by a magnetic field along a low-symmetry direction which causes the little-group *irreps* at the high-symmetry k -points of $Pa\bar{3}$ to decompose into *irreps* of $P\bar{1}$ (see Supplementary Section 5). The SI of $P\bar{1}$, with a $\mathbb{Z}_2^3 \times \mathbb{Z}_4$ group structure, can be calculated using the inversion symmetry eigenvalues at the 8 high-symmetry momenta of $P\bar{1}$ ³², and their possible values are shown in Table 1 where they are written as a quadruplet set of the numbers $\mathbb{Z}_{2,x}\mathbb{Z}_{2,y}\mathbb{Z}_{2,z}\mathbb{Z}_4$. Upon this symmetry breaking, the different energetic ordering of magnon *irreps* at the different high-symmetry momenta of $P\bar{1}$ always ensures at least one magnon energy gap (specifically, the middle gap) with a topological SI ¹⁵ as shown in Table 1. The $\mathbb{Z}_{2,i=x,y,z}$ index diagnoses the Chern number *modulo* 2 on the $k_i = 0, \pi$ planes and the \mathbb{Z}_4 index diagnoses the difference between the Chern numbers on the two high-symmetry planes $k_z = 0, \pi$. Consequently, the SI value 1112 of the second gap reveals an even number of perturbation-induced topologically nontrivial Weyl crossings in half of the Brillouin zone between the second and third magnon bands at generic momenta.

Table 1: Possible values for the SI in each band gap¹⁵ after symmetry breaking from supergroup $Pa\bar{3}$ into subgroup $P\bar{1}$. Gap i refers to the band gap between the i -th and $(i + 1)$ -th lowest energy bands. Green SI s mark the realized values in a field of 14 T along the low-symmetry direction [0 1 6] using the spin model obtained from fitting INS and Raman data. Findings of this paper does not depend on the details of the used low-symmetry magnetic field. The field strength of 14 T was adopted to induce a measurable middle band gap opening in future in-field INS experiments. The fourth gap refers to the collection of all four magnon bands which is always trivial. More technically, it is an elementary band representation^{12,15} induced from the local “orbitals” S_i^\pm .

Gap#	Possible SI Values
1	0000, 0003, 0010, 0011, 0012
	0013, 0100, 0101, 0102, 0103
	0110, 0111, 0112, 0113, 1000
	1001, 1002, 1003, 1010, 1011
	1012, 1013, 1100, 1101, 1102
	1103, 1112, 1113
	1112
2	0000, 0001, 0010, 0011, 0012
	0013, 0100, 0101, 0102, 0103
	0110, 0111, 0112, 0113, 1000
	1001, 1002, 1003, 1010, 1011
	1012, 1013, 1100, 1101, 1102
	1103, 1111, 1112
	1112
3	0000, 0001, 0010, 0011, 0012
	0013, 0100, 0101, 0102, 0103
	0110, 0111, 0112, 0113, 1000
	1001, 1002, 1003, 1010, 1011
	1012, 1013, 1100, 1101, 1102
	1103, 1111, 1112
	1112
4	0000
	0000
	0000
	0000
	0000
	0000
	0000

Inelastic Neutron and Magneto-Raman Scattering

High-quality cm-sized single crystals of $MnTe_2$ were grown through a Bridgman process (Supplementary Fig. 1) and confirmed to order antiferromagnetically below 87 K (Supplementary Fig. 2). INS experiments were performed to reveal the full magnon band structure. Fig. 1 (c) illustrates the experimentally measured magnon dispersion along high symmetry directions as collected by single crystal INS.

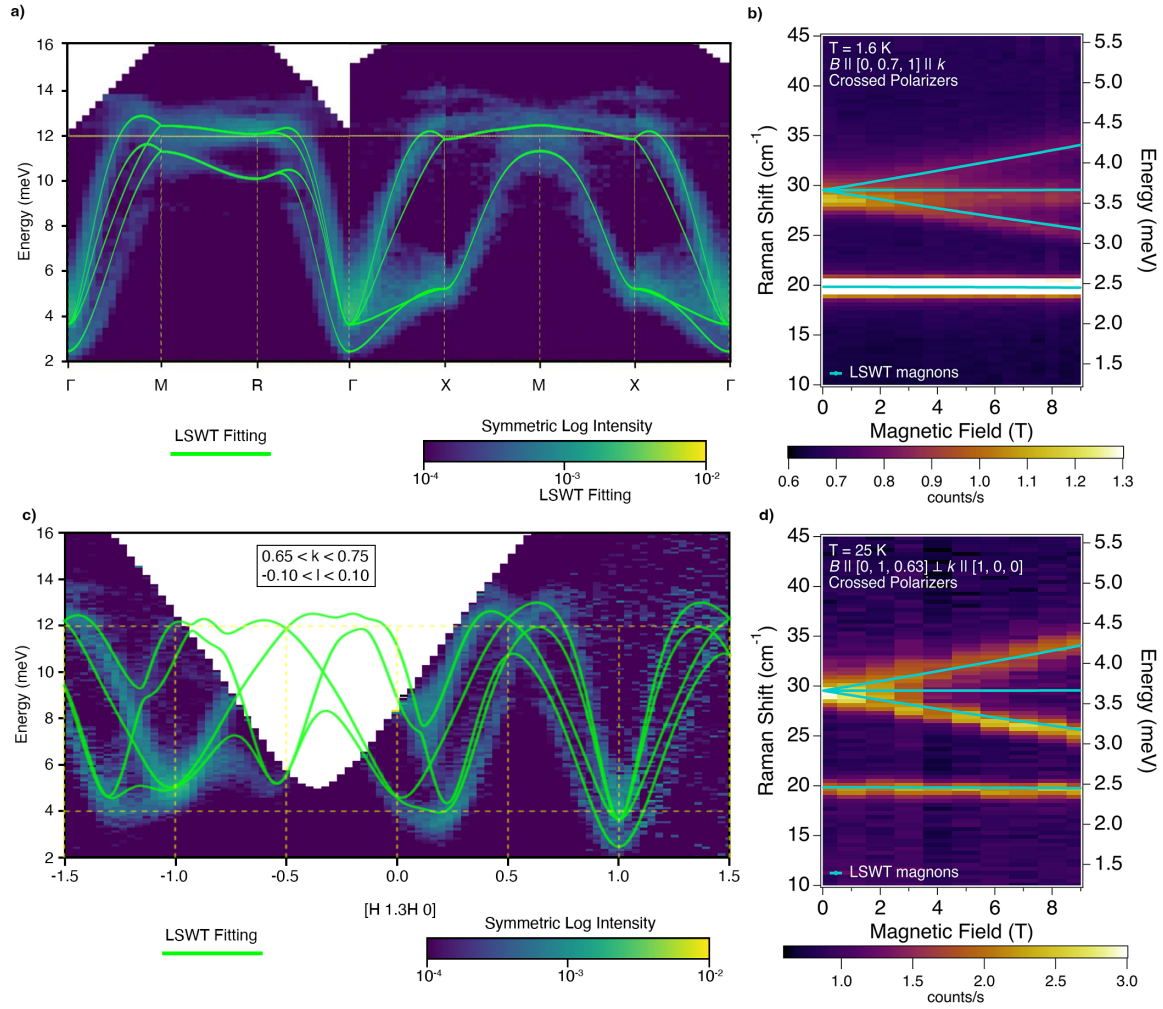


Figure 2: Probing magnon band structure of MnTe₂. a,c) An overlay of the LSWT fitting of the magnonic spectra over the experimental INS data along (a) the high symmetry directions in the Brillouin zone and a (c) low symmetry direction $[K 0.2 + 1.3K 0]$. Refer to Supplementary Figs. 3-6 for more detailed comparison between LSWT simulations and INS measurements. b) Magneto-Raman data collected in the Faraday configuration with the field applied along $[0 0.7 1]$ parallel to the light propagation direction. d) Magneto-Raman data collected in the Voigt configuration, with the field $B \parallel [0 1 0.63]$ and the light propagation along $[1 0 0]$.

Measurements were collected at 5 K with 22 meV incident energy at the SEQUOIA beamline of the Spallation Neutron Source. The zone center magnons energies are 2.5 ± 0.2 meV and 4.1 ± 0.5 meV at zero magnetic field. Both modes have a steep dispersion resulting in two broad doubly-degenerate modes, as indicated by the band representation analysis, from Γ to M that occur at 11.1 ± 0.5 meV and 12.2 ± 0.5 meV. At high momentum, from M to R , two low-intensity modes appear above and below a flat magnon dispersion along this direction. These modes are most likely phonon modes as the DFT calculations of the phonon dispersion show modes at these energies and momenta (details in the Supplementary Section 6). In addition, these are seen only at high momentum transfer as expected given that, in a neutron experiment, phonons increase in intensity with momentum transfer Q as Q^2 . Along the Γ to X direction, a crossover is seen as one band of the triply-degenerate state at Γ joins the lower energy mode while the other two modes remain degenerate and disperse to higher energies. At these high symmetry points of the Brillouin zone, the degeneracies of the magnons follow the predictions of the symmetry analysis presented in the previous section (see Fig. 3 (a)).

Raman experiments, performed at 1.6 K and 120 K, showed the presence of two magnon modes at the Brillouin zone center Γ (Fig. 1 (d), Supplementary Fig. 9) in the magnetically ordered state and at zero magnetic field. At both temperatures four zone center phonons are identified at the energies of 12.1 ± 0.2 meV, 13.3 ± 0.2 meV, 22.2 ± 0.1 meV, and 22.7 ± 0.2 meV, which match well with previous reports on MnTe₂³³, and are labeled A through D in Fig. 1(d) with symmetries noted in parenthesis. Notably, the B mode, with *irrep* $^1E_g + ^2E_g$, seems to be split in the low temperature phase, where the two modes are labeled as B and B'. This splitting occurs because of the loss of time-reversal symmetry with the magnetic order removing the degeneracy of these time-reversal phonon pairs. Two magnons, labeled as M_1 and M_2 in Fig. 1(d), appear in the 1.6 K scan at 2.5 ± 0.1 meV and 3.5 ± 0.1 meV, in agreement with the INS data. These two modes soften and disappear as expected when approaching the ordering temperature (Supplementary Fig. 10).

Additional Raman measurements in a magnetic field show that the 2.5 meV mode is singly degenerate, while the 3.5 meV mode is triply degenerate and is split into three modes by a magnetic field applied along the low symmetry direction $[0 0.7 1]$, as shown in Fig. 2(b). We recognize the *irreps* for the magnons as 1E_g and T_g , respectively. When the field is applied along this low symmetry direction, the MSG is reduced to $P\bar{1}$, and all degeneracies of the magnon wavefunctions are broken, causing the triply degenerate magnon to split into three separate magnons with the same *irreps* A_g . In the Faraday configuration of this experiment where $k \parallel B \parallel [0 0.7 1]$, all three

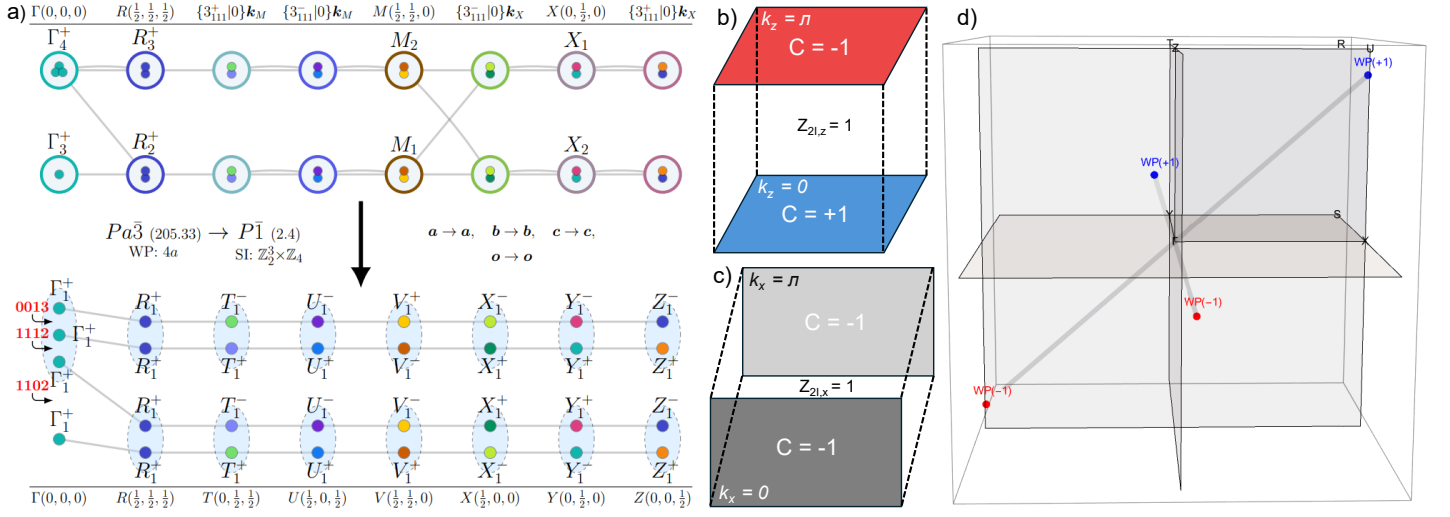


Figure 3: Topological Weyl magnonic excitations in MnTe₂. a) Schematic representation of the magnon band structure of MnTe₂ upon symmetry reduction from parent $MSG Pa\bar{3}$ into the subgroup $P\bar{1}$. The lower part manifests the explicit magnon band *irreps* calculated using the obtained spin Hamiltonian. b-c) Demonstration of the calculated Chern numbers of the upper two bands over high-symmetry planes upon symmetry breaking, consistent with the SZ predictions, thus requiring non-trivial bands to occur. d) Weyl points in k -space upon the application of a 14 T magnetic field along the $[0\ 1\ 6]$ direction.

components of the T_g mode have non-zero Raman response. On the other hand, in the Voigt configuration experiment where $k \parallel (100)$ and is perpendicular to $B \parallel [0\ 1\ 0.63]$, shown in fig.2(d), only two of the three modes are observable due to the form on the Raman tensors of the T_g *irreps* of the $MSG Pa\bar{3}$ shown in Supplementary Section 7.

Hamiltonian Modeling

The INS and magneto-Raman data show highly coherent quasiparticles suggesting that linear spin wave theory (LSWT) can model the spin dispersion correctly. We have extracted a spin model that is consistent with all experimental data to explicitly understand its magnon excitations and further refine our predictions of the magnon topology exhibited in this material. The non-coplanar structure of MnTe₂ can be stabilized with an antisymmetric spin-spin nearest-neighbor exchange interaction such as the Dzyaloshinsky-Moriya interaction (DMI). We then searched for values of the Heisenberg exchange interactions J_i and the DMI D by fitting the LSWT calculations to both the INS spectrum and magnetic field dependence obtained from magneto-Raman measurements. In order to adequately match the observed spin excitations, weaker longer-ranged spin-spin interactions up to the 5th nearest neighbors have to be included (Fig. 2a). The overall spin Hamiltonian takes the form:

$$\hat{H} = \sum_{\langle i,j \rangle} [J_1 \hat{S}_i \cdot \hat{S}_j + \vec{D} \cdot \hat{S}_i \times \hat{S}_j] + \sum_{\langle i,j \rangle_{n=2}}^5 J_n \hat{S}_i \cdot \hat{S}_j + g \mu_B \sum_i \vec{B} \cdot \hat{S}_i \quad (2)$$

where J_1 is the first nearest neighbor (NN) Heisenberg bond, \vec{D} is the NN DMI vector, $J_{n \in \{2, \dots, 5\}}$ are the n -th NN bonds, $g = 2$ is the Landé g -factor, μ_B is the Bohr magneton, and \vec{B} is an externally applied magnetic field.

J_1	D_z	D_y	D_x	J_2	J_3^1
0.5922(139)	0.09901(281)	0.08356(151)	-0.0027456(80)	-0.11943(340)	-0.05712(169)
	J_3^2	J_4^1	J_4^2	J_5^1	J_5^2
	-0.08659(245)	-0.020076(577)	-0.07905(221)	0.12331(364)	0.010620(314)

Table 2: Spin model interaction parameters (in meV). Uncertainties represent standard deviation of an ensemble of parameter sets generated by randomly perturbing the best-fit values within $\pm 5\%$ and retaining only those realizations with a total loss within 15% of the minimum. The reported means and standard deviations thus represent the local variability of parameters consistent with *near-optimal fits*. Bonds, shown in Fig. 1(b), of the same length are denoted by superscripts.

As shown in Fig. 2 and Supplementary Figs. 3 – 6, excellent agreement with both INS and magneto-Raman data is obtained via the parameter set in Table 2. For instance, the spin model is able to accurately fit the the high-symmetry Brillouin zone map (Fig. 2a), as well as an arbitrarily chosen low-symmetry direction $[H\ 0.6 + 1.3H\ 0]$, (Fig. 2c). Furthermore, the spin model is able to reproduce the splitting of the three-fold degenerate 3.5 meV Γ -point magnon mode in the Raman spectra, when a magnetic field is applied along the $[0\ 0.7\ 1]$ direction (Fig. 2b). This was further confirmed when the magnetic field was applied along $[0\ 1\ 0.63]$ (Fig. 2d). The magnitudes of the

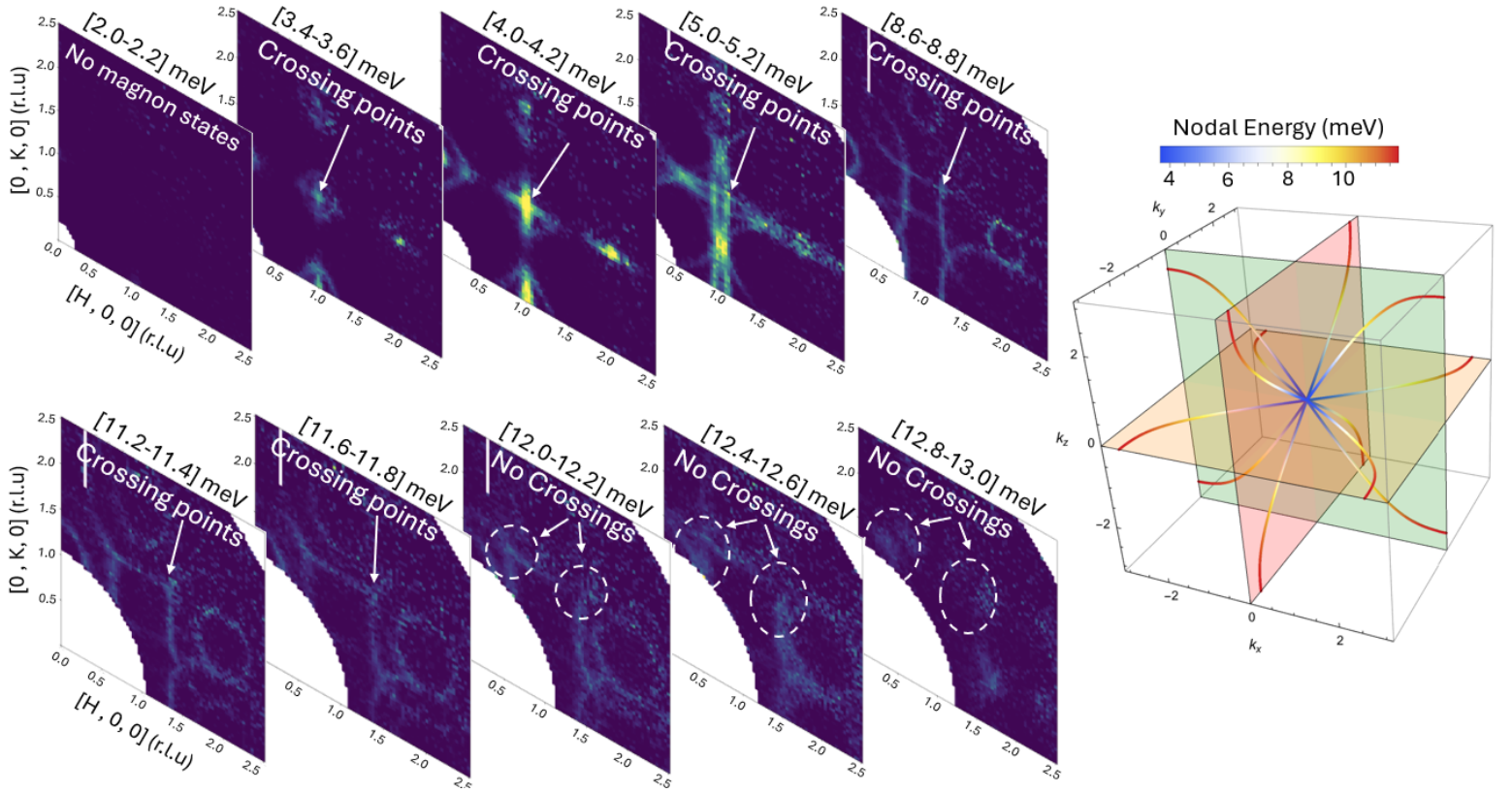


Figure 4: Magnon nodal lines in unperturbed MnTe_2 . Zero-field INS energy scans on the $k_z = 0$ plane covering the energy range of the nodal lines, whose energy-momentum structure is calculated using LSWT on the right panel. Lowest energy of the nodal lines start to appear from ~ 3.6 meV at the zone center, and shift away from the zone center towards the $M(1/2, 1/2, 0)$ (and its symmetry-equivalent) points as energy increases. A white arrow on INS scans refers to one of the symmetry-related crossing points. Above the highest energy part of the nodal lines at ~ 11.76 meV, the crossing points between the iso-energy contours start to gap out, as evident in the INS scans above 12 meV.

exchange constants in the spin model suggest dominant nearest neighbor spin-spin interaction, finite DMI stabilizing the non-coplanarity of the magnetic structure, and weaker interactions over the longer bonds.

Magnon Band Topology

Magnon band topology calculations were performed using the obtained spin Hamiltonian with an additional magnetic field along a low-symmetry direction, which we take to be along $[0\ 1\ 6]$. First, we calculate the inversion eigenvalues of the magnon eigenfunctions at the eight high-symmetry momenta, as presented in the lower part of Fig. 3(a). From this, the calculated $\mathcal{S}\mathcal{I}$ s were confirmed to belong to the values predicted by band representations¹⁵. In particular, we find that the second and third magnon bands cross at some generic momenta in the BZ, and therefore we can interpret the middle gap $\mathcal{S}\mathcal{I}$ value 1112 as following. First, the $\mathbb{Z}_{2,i}$ index indicates that the Chern number of the combined upper two bands takes a value of $1 \bmod 2$ on the high symmetry planes $k_i = 0, \pi$ for $i = x, y, z$. This is confirmed explicitly in our model as seen in Fig. 3 (b,c), calculated using the numerical technique developed in Ref.³⁴. Second, the \mathbb{Z}_4 index indicates a difference of 2 between the Chern numbers on the $k_z = 0, \pi$ planes. This is an indication of a gap closing and an existence of an even number of Weyl magnons in between these two high symmetry planes. Additionally, the chiralities of these Weyl magnons are such that they give rise to the difference of the Chern numbers on these two planes.

Throughout, we focus on the second energy band gap for two reasons: first, this topological band gap^{12,15} occurs for all possible spin models, and second, it is also larger than the first and third band gaps. The subgroup $P\bar{1}$ is special in the sense that regardless of the order of the magnon band *irreps* of $Pa\bar{3}$, they will always decompose into *irreps* of $P\bar{1}$ with a topological gap between the second and third magnon bands. The upper panel of Fig. 3(a) shows a schematic representation of the magnon band *irreps* which, upon applying the appropriate perturbation to break into $P\bar{1}$, are decomposed into *irreps* of $P\bar{1}$ such that the middle gap is always topological as discussed above. The calculated $\mathcal{S}\mathcal{I}$ s of the induced band gaps using our spin model are shown in the lower panel of Fig. 3(a). Scanning the BZ between the second and third bands, we identified two Weyl crossings at generic momenta $\mathbf{k} = (0.4964, 0.0031, 0.4333), (-0.04969, 0.2142, 0.1518)$ in units of $2\pi/a$, where a is the lattice constant, at energies 11.75 meV and 7.48 meV, in a magnetic field of 14 T along $[0\ 1\ 6]$. Their topological charges, calculated as the Chern number on a small sphere enclosing the crossing point are $+1, +1$, and are consistent with the Chern numbers on the high-symmetry planes $k_i = 0, \pi$ for $i = x, y, z$. Inversion symmetry enforces their opposite-chirality partners to lie at the opposite momenta. Fig. 3 (d) shows the position of the two Weyl pairs. In the absence of a magnetic field, the $M\mathcal{S}\mathcal{G}$ contains three glide symmetries $\{m_{100}|\frac{1}{2}\frac{1}{2}0\}$, $\{m_{010}|\frac{1}{2}\frac{1}{2}0\}$, and $\{m_{001}|\frac{1}{2}\frac{1}{2}0\}$ that protect magnon nodal lines³⁵ on the glide-symmetric planes $k_i = 0$ for $i = x, y, z$ (more details in Supplemental Section 4), as validated by the spin wave calculation and confirmed with the INS data as presented in Fig. 4. The topology of these nodal lines is confirmed in terms of a nonzero Berry phase of $\pi \pmod{2\pi}$ of the upper two bands on a closed contour that encircles the magnon nodal lines. By tracing the locations of the Weyl magnons (shown in Fig. 3 (d)) as

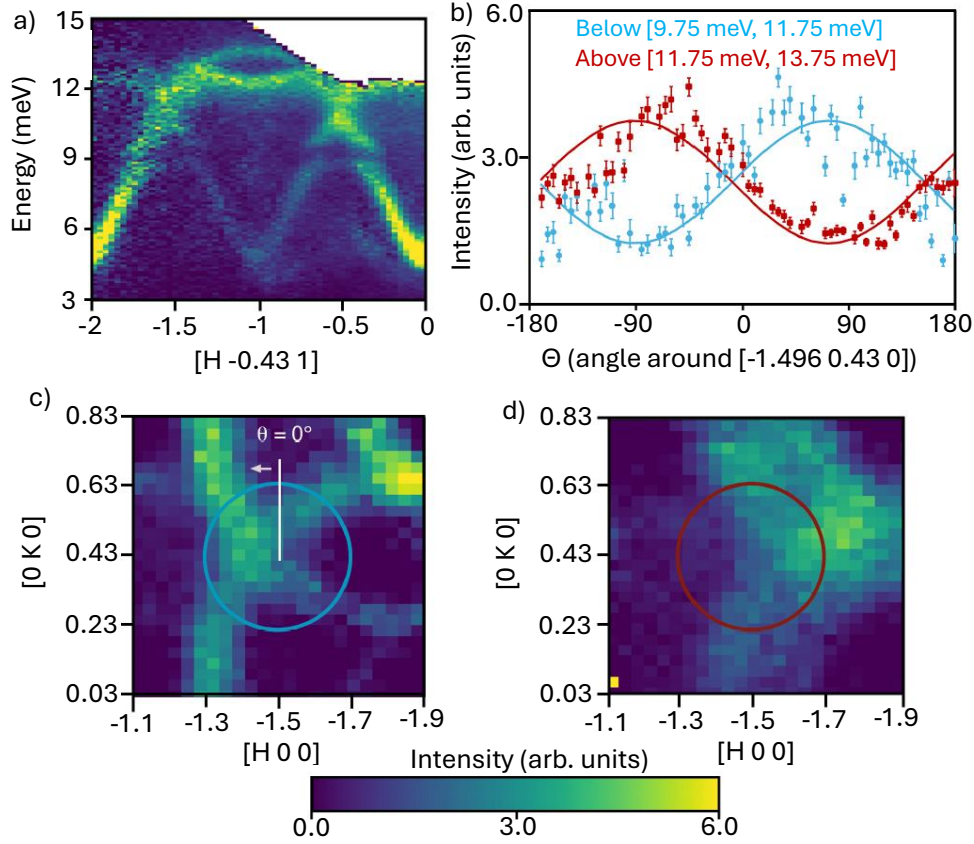


Figure 5: INS intensity winding associated with the magnon nodal lines. (a) Magnon dispersion along the $[H -0.429 1]$ line that intersects the nodal lines at the $(-1.50 0.429 0)$ k -points. (b-d) INS intensity integrated over a finite energy range of 2 meV above (red) and below (blue) the energy of the crossing at $(-1.50 0.429 0)$ as a function of angle α around the crossing point. Data points are annotated with error bars that illustrate one standard deviation of the intensity. The solid lines are a refined sinusoidal fit to demonstrate the bimodal intensity pattern. k_x vs. k_y plots, at $k_z = 0$, centered on the nodal crossing $(-1.50 0.429 0)$ demonstrating the energy dependence below (c) and above (d) the nodal crossing. The overlaid circles demonstrate the region of integration for the plot in (b) with the colors matching the below and above designation in (b). The white line in (c) indicates the starting orientation of $\alpha = 0$ and the direction in which α increases.

the magnetic field is turned off, we find that Weyl pairs move in the BZ towards the high-symmetry planes until they return and become part of the nodal lines at zero field. In other words, as the magnetic field is turned on, the zero-field nodal lines gap out and the two Weyl magnon pairs emerge.

A direct experimental signature of the magnon nodal lines at zero field is the way in which the INS intensity changes around a loop in momentum space for energy ranges above and below it as established in Ref.³⁶ for arbitrary magnon two-band touching points. This winding behavior is directly related to the non-trivial topology of the magnon wavefunction near the nodal crossing, and has been verified experimentally for the case of Dirac magnons^{27,30} and Dirac nodal lines²⁵. We demonstrate this behavior here, as a result of the nonzero Berry phase around the nodal lines, by focusing on a point that belongs to one of the nodal lines at zero field, the $(0.5, 0, 0.429)$ point (see Fig. 5 (a,b)), and analyze the INS intensity on two constant energy intervals, one below and one above the energy of the nodal crossing. As shown in Fig. 5 (c,d), the INS intensity follows a sinusoidal modulation while winding around the nodal cone for an energy range above the node energy, and follows an opposite winding for a lower energy range (Fig 5b). To illustrate the sinusoidal behavior, the INS data within the overlaid circles (see Fig. 5 (c,d)) are flattened and the INS intensity is plotted as a function of α defined in Fig 5 (b). Sinusoidal fits that are phase-shifted by π demonstrate great agreement with the experimental intensity.

Conclusion

We have established that the non-coplanar antiferromagnet MnTe_2 is a material host for topological nodal line magnons in zero field and Weyl magnons at finite field. Through a combination of INS, magneto-Raman measurements, and theoretical calculations we probed the magnon band structure of MnTe_2 , determined the microscopic spin Hamiltonian, confirmed the existence of topological magnon nodal lines enforced by the \mathcal{MSG} symmetries, and analyzed the emergence of Weyl magnons induced by an external magnetic field. This discovery not only establishes a concrete bosonic analogue of Weyl fermions but also provides a promising platform for exploring tunable topological excitations and associated transport phenomena in magnetic systems. Our results serve as the foundation for future investigations of direct in-field INS imaging of Weyl magnons, their associated bulk thermal transport³⁷ and surface magnons, and possible device applications based on topological spin transport⁷. This realization of a tunable Weyl magnon phase highlights the rich interplay between magnetic order and band topology in non-coplanar antiferromagnets and demonstrates the power of combining the symmetry based topological analysis with appropriate experiments in the discovery of new topological magnon materials.

Methods

The inelastic neutron scattering experiments were performed on the Fine-Resolution Fermi Chopper Spectrometer³⁸ at the Spallation Neutron Source, Oak Ridge National Laboratory. A 1.7 g single crystal of pure MnTe₂ was used with incident neutron energies of $E_i = 22$ meV. The chopper configuration consisted of the T-zero chopper operating at 60 Hz and the instruments standard fine resolution Fermi chopper operating at 240 Hz. This configuration has a calculated full width at half maximum (FWHM) energy resolution 0.55 meV for elastically scattered neutrons and 0.41 meV at 10 meV energy transfer. Measurements were performed at $T = 5$ K. The crystal was aligned prior to the experiment using a backscattering Laue X-ray diffractometer. The crystal was aligned in the (HK0) scattering plane at the neutron spectrometer. Alignment scans were performed with 81.81 meV incident energy neutrons with the sample at $T = 5$ K. The full width at half maximum intensity of the nuclear peak rocking curves was measured as 0.78 degrees for the (4 0 0) and 0.88 degrees for the (0 -4 0) reflection respectively. The measured energy resolution of elastically scattered neutrons using the nuclear incoherent scattering of the sample was found to be 0.61 meV FWHM. The crystal was mounted in an aluminum sample can and sealed under an atmosphere of He gas. A neutron-absorbing Cd foil was placed at the bottom of the sample can and in the vicinity of the sample mounting hardware to reduce the neutron scattering background from the sample holder. In order to access a volume of reciprocal space with the instruments highly pixelated detector, the sample was rotated about its vertical axis over a range of 140 degrees with a step size of 0.5 degrees. Individual angles of this rotation were measured for between 0.47 and 1.67 Coulombs of charge on the spallation neutron source target. This corresponds to between 6 and 21 minutes of data collection for each angle measured. The data were histogrammed using the SHIVER software and were folded into the first Brillouin zone of the simple cubic $Pa\bar{3}$ space group of MnTe₂ to improve counting statistics.

Magneto-Raman scattering at NIST was done using a 632 nm He-Ne laser with a triple grating spectrometer which has a resolution around 0.4 cm^{-1} . Experiments in both Faraday and Voigt geometries ($k \parallel B$ and $k \perp B$, respectively) were performed. The sample is mounted in a cryostat which cools down the sample from room temperature to around 1.6K with the sample in a He exchange gas environment. This system is also able to apply an external magnetic field up to 9 T. Polarization optics were used in both the incoming and outgoing beams, allowing linear polarization analysis. The parallel polarizers configuration results are acquired by rotating a half-wave plate in front of the sample. Laser power was maintained at $300 \mu\text{W}$ for the $B \parallel (0 0.7 1)$ and at $150 \mu\text{W}$ for the $B \parallel (0 1 0.63)$ experiments to avoid any possible damage.

Acknowledgments

AEF acknowledges a useful discussion with Prof. Manuel dos Santos Dias (STFC Daresbury Laboratory). This work was primarily funded by the National Science Foundation MRSEC program under grant DMR-2011876 to the Center for Emergent Materials at Ohio State. The identification of any commercial product or trade name does not imply endorsement or recommendation by the National Institute of Standards and Technology. This research used resources at the Spallation Neutron Source, a DOE Office of Science User Facility operated by the Oak Ridge National Laboratory. The beam time was allocated to SEQUOIA (BL- 17) on proposal number IPTS-32637.1.

Author Contributions

Theoretical framework, spin model construction, linear spin wave calculations, and magnon band topology analysis were carried out by AEF, with supervision from MJK and YML. The Hamiltonian fitting of the INS and Raman experiments was done by AEF and YL. Neutron scattering experiments were performed by AJW, MBS, and JEG. Raman measurements were carried out by YL, TTM, RVA, and ARHW. DFT calculations were done by KFG. X-ray diffraction was performed by AJW and JEG. The manuscript was written by AEF, AJW, RVA, JEG and YL and was edited by all authors. All authors contributed to the project development discussions.

References

- [1] Shindou, R., Matsumoto, R., Murakami, S. & Ohe, J.-i. Topological chiral magnonic edge mode in a magnonic crystal. *Physical Review B* **87**, 174427 (2013).
- [2] Mook, A., Henk, J. & Mertig, I. Edge states in topological magnon insulators. *Physical Review B* **90**, 024412 (2014).
- [3] McClarty, P. A., Kruger, F., Guidi, T. & Parker, D. Topological magnons: a review. *Annual Review of Condensed Matter Physics* **12**, 179–200 (2021).
- [4] Shindou, R., Matsumoto, R., Murakami, S. & Ohe, J.-i. Topological chiral magnonic edge mode in a magnonic crystal. *Phys. Rev. B* **87**, 174427 (2013). URL <https://link.aps.org/doi/10.1103/PhysRevB.87.174427>.
- [5] Halperin, B. I. Quantized hall conductance, current-carrying edge states, and the existence of extended states in a two-dimensional disordered potential. *Phys. Rev. B* **25**, 2185–2190 (1982). URL <https://link.aps.org/doi/10.1103/PhysRevB.25.2185>.
- [6] Cornelissen, L. J., Liu, J., Duine, R. A., Youssef, J. B. & van Wees, B. J. Long-distance transport of magnon spin information in a magnetic insulator at room temperature. *Nature Physics* **11**, 1022–1026 (2015). URL <http://dx.doi.org/10.1038/nphys3465>.
- [7] Chumak, A. V., Vasyuchka, V. I., Serga, A. A. & Hillebrands, B. Magnon spintronics. *Nature Physics* **11**, 453–461 (2015).
- [8] Nakata, K., Kim, S. K. & Tserkovnyak, Y. Magnonic topological insulators in antiferromagnets. *Physical Review B* **96**, 224414 (2017).
- [9] Wang, H., Su, Y. & Wang, X. R. Topological magnonics: a paradigm for spin-wave manipulation and device design. *Physical Review B* **97**, 134421 (2018).

- [10] Mook, A., Henk, J. & Mertig, I. Tunable magnon weyl points in ferromagnetic pyrochlores. *Phys. Rev. Lett.* **117**, 157204 (2016). URL <https://link.aps.org/doi/10.1103/PhysRevLett.117.157204>.
- [11] Li, F.-C., Li, G.-Y., Zhang, G., Li, J. & Gong, S.-S. Weyl magnons in breathing pyrochlore antiferromagnets. *Nature Communications* **12**, 3120 (2021).
- [12] Karaki, M. J. *et al.* An efficient material search for room-temperature topological magnons. *Science Advances* **9**, eade7731 (2023). URL <https://www.science.org/doi/abs/10.1126/sciadv.ade7731>. <https://www.science.org/doi/pdf/10.1126/sciadv.ade7731>.
- [13] Su, Y., Wang, X. S. & Wang, X. R. Magnonic weyl semimetal and chiral anomaly in pyrochlore ferromagnets. *Phys. Rev. B* **95**, 224403 (2017). URL <https://link.aps.org/doi/10.1103/PhysRevB.95.224403>.
- [14] Owerre, S. A. Weyl magnons in noncoplanar stacked kagome antiferromagnets. *Physical Review B* **97** (2018). URL <http://dx.doi.org/10.1103/PhysRevB.97.094412>.
- [15] Karaki, M. J. *et al.* High-throughput discovery of perturbation-induced topological magnons. *npj Computational Materials* **11** (2025). URL <http://dx.doi.org/10.1038/s41524-025-01706-2>.
- [16] Xu, S.-Y. *et al.* Discovery of a weyl fermion semimetal and topological fermi arcs. *Science* **349**, 613–617 (2015). URL <http://dx.doi.org/10.1126/science.aaa9297>.
- [17] Lv, B. Q. *et al.* Experimental discovery of weyl semimetal taas. *Phys. Rev. X* **5**, 031013 (2015). URL <https://link.aps.org/doi/10.1103/PhysRevX.5.031013>.
- [18] Lu, L. *et al.* Experimental observation of weyl points. *Science* **349**, 622–624 (2015). URL <http://dx.doi.org/10.1126/science.aaa9273>.
- [19] Li, F., Huang, X., Lu, J., Ma, J. & Liu, Z. Weyl points and fermi arcs in a chiral phononic crystal. *Nature Physics* **14**, 30–34 (2018).
- [20] Wan, X., Turner, A. M., Vishwanath, A. & Savrasov, S. Y. Topological semimetal and fermi-arc surface states in the electronic structure of pyrochlore iridates. *Phys. Rev. B* **83**, 205101 (2011). URL <https://link.aps.org/doi/10.1103/PhysRevB.83.205101>.
- [21] Burkov, A. A. Anomalous hall effect in weyl metals. *Phys. Rev. Lett.* **113**, 187202 (2014). URL <https://link.aps.org/doi/10.1103/PhysRevLett.113.187202>.
- [22] Mook, A., Henk, J. & Mertig, I. Thermal hall effect in noncollinear coplanar insulating antiferromagnets. *Phys. Rev. B* **99**, 014427 (2019). URL <https://link.aps.org/doi/10.1103/PhysRevB.99.014427>.
- [23] Chisnell, R. *et al.* Topological magnon bands in a kagome lattice ferromagnet. *Phys. Rev. Lett.* **115**, 147201 (2015). URL <https://link.aps.org/doi/10.1103/PhysRevLett.115.147201>.
- [24] Chisnell, R. *et al.* Magnetic transitions in the topological magnon insulator $\text{Cu}(1,3\text{-bdc})$. *Phys. Rev. B* **93**, 214403 (2016). URL <https://link.aps.org/doi/10.1103/PhysRevB.93.214403>.
- [25] Elliot, M. *et al.* Order-by-disorder from bond-dependent exchange and intensity signature of nodal quasiparticles in a honeycomb cobaltate. *Nature Communications* **12** (2021). URL <http://dx.doi.org/10.1038/s41467-021-23851-0>.
- [26] Chen, L. *et al.* Topological spin excitations in honeycomb ferromagnet CrI_3 . *Phys. Rev. X* **8**, 041028 (2018). URL <https://link.aps.org/doi/10.1103/PhysRevX.8.041028>.
- [27] Nikitin, S. E. *et al.* Thermal evolution of dirac magnons in the honeycomb ferromagnet CrBr_3 . *Phys. Rev. Lett.* **129**, 127201 (2022). URL <https://link.aps.org/doi/10.1103/PhysRevLett.129.127201>.
- [28] Yao, W. *et al.* Topological spin excitations in a three-dimensional antiferromagnet. *Nature Physics* **14**, 1011–1015 (2018). URL <http://dx.doi.org/10.1038/s41567-018-0213-x>.
- [29] Bao, S. *et al.* Discovery of coexisting dirac and triply degenerate magnons in a three-dimensional antiferromagnet. *Nature Communications* **9** (2018). URL <http://dx.doi.org/10.1038/s41467-018-05054-2>.
- [30] Scheie, A. *et al.* Dirac magnons, nodal lines, and nodal plane in elemental gadolinium. *Phys. Rev. Lett.* **128**, 097201 (2022). URL <https://link.aps.org/doi/10.1103/PhysRevLett.128.097201>.
- [31] Peng, B., Jiang, Y., Fang, Z., Weng, H. & Fang, C. Topological classification and diagnosis in magnetically ordered electronic materials. *Phys. Rev. B* **105**, 235138 (2022). URL <https://link.aps.org/doi/10.1103/PhysRevB.105.235138>.
- [32] Peng, B., Jiang, Y., Fang, Z., Weng, H. & Fang, C. Topological classification and diagnosis in magnetically ordered electronic materials. *Physical Review B* **105** (2022). URL <http://dx.doi.org/10.1103/PhysRevB.105.235138>.
- [33] Müller, B. & Lutz, H. Raman spectra of MnSe_2 , MnTe_2 , RuTe_2 , and OsTe_2 . *Solid State Communications* **78**, 469–471 (1991). URL <https://www.sciencedirect.com/science/article/pii/0038109891907062>.
- [34] Fukui, T., Hatsugai, Y. & Suzuki, H. Chern numbers in discretized brillouin zone: Efficient method of computing (spin) hall conductances. *Journal of the Physical Society of Japan* **74**, 1674–1677 (2005). URL <http://dx.doi.org/10.1143/JPSJ.74.1674>.
- [35] Fang, C., Weng, H., Dai, X. & Fang, Z. Topological nodal line semimetals. *Chinese Physics B* **25**, 117106 (2016). URL <https://dx.doi.org/10.1088/1674-1056/25/11/117106>.
- [36] Shivam, S., Coldea, R., Moessner, R. & McClarty, P. Neutron scattering signatures of magnon weyl points (2017). URL <https://arxiv.org/abs/1712.08535>.
- [37] Onose, Y. *et al.* Observation of the magnon hall effect. *Science* **329**, 297–299 (2010). URL <http://dx.doi.org/10.1126/science.1188260>.

- [38] Granroth, G., Vandergriff, D. & Nagler, S. Sequoia: A fine resolution chopper spectrometer at the sns. *Physica B: Condensed Matter* **385-386**, 1104–1106 (2006). URL <https://www.sciencedirect.com/science/article/pii/S0921452606012701>.

Weyl Magnons in the Non-Coplanar Antiferromagnet MnTe₂: *Supplementary Materials*

Ahmed E. Fahmy^{1,*}, Archibald J. Williams^{2,*}, Yufei Li^{1,*}, Thuc Mai³, Kevin F. Garrity³, Matthew B. Stone⁴, Mohammed J. Karaki¹, Sara Haravifard^{5,6}, Angela R. Hight Walker³, Rolando Valdes Aguilar¹, Joshua E. Goldberger², and Yuan-Ming Lu¹

¹*Department of Physics, The Ohio State University, Columbus, OH 43210, USA*

²*Department of Chemistry and Biochemistry, The Ohio State University, Columbus, OH 43210, USA*

³*Quantum Measurements Division, Physical Measurement Laboratory, National Institute of Standards and Technology, Gaithersburg, MD 20899, USA*

³*Department of Physics, Duke University, Durham, North Carolina 27708, USA*

⁴*Neutron Scattering Division, Oak Ridge National Laboratory, Oak Ridge, Tennessee 37831, United States of America*

⁵*Department of Physics, Duke University, Durham, North Carolina 27708, USA*

⁶*Department of Mechanical Engineering and Materials Science, Duke University, Durham, North Carolina 27708, USA*

*These authors contributed equally to this work.

Contents

1 Crystal Growth	1
1.1 Synthesis	1
1.2 Structural Characterization	1
2 Magnetic Measurements	2
3 Linear Spin Wave Theory	2
4 Magnon Nodal Lines	3
5 Topology of Middle Magnon Band Gap	5
6 DFT Calculation	6
7 Raman Polarization and Temperature Dependence	7

1 Crystal Growth

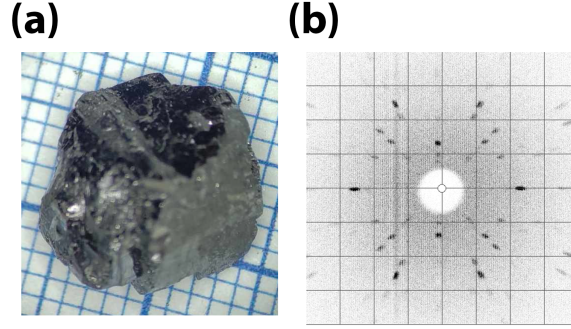
1.1 Synthesis

Single crystals of MnTe₂ were grown from a Bridgman type growth using Te self-flux. Mn powder (99.95%, Thermo Scientific) and Te lump (99.9999%, Thermo Scientific) were mixed together in a 1:4 molar ratio and ground to a coarse powder at a typical total scale of 20 g. This mixture was added to a quartz ampoule under an Ar atmosphere and sealed under <80 mTorr. To maximize single crystal growth, these ampoules were closed with a tapered end rather than a rounded end, and the bottom of the tube was graphitized with isopropyl alcohol. The tube was hung in a vertical single-zone furnace by the procedure outlined in¹. The ampoule was heated to 850 °C over 24 hours and held at temperature for 50 hours to allow homogenization. The tube was then dropped at 5.79 μL/hr or the equivalent of 0.33 mm/hr over 330 hours before allowing to cool to room temperature over 12 hours. Single crystals of MnTe₂ (Supplementary Fig. 1a) were extracted from the flux through the use of a razor blade.

1.2 Structural Characterization

Phase purity of the grown MnTe₂ crystals was confirmed by grinding grown crystals into a powder for analysis using powder X-ray diffraction. Powder X-ray diffraction measurements were performed on a Bruker D8 Advance powder X-ray diffractometer using Cu K_{α1} radiation that was generated at 40 kV and 40 mA.

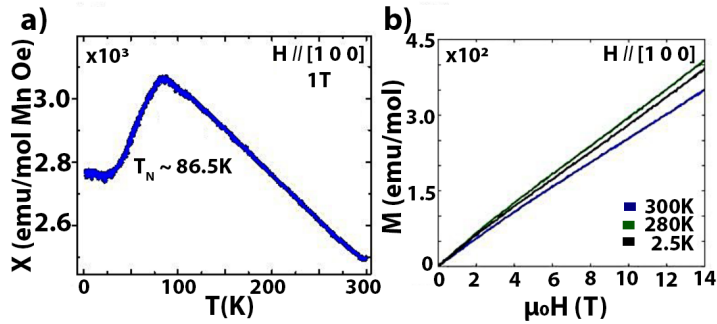
Single crystallinity across the grown crystals was confirmed by Laue backscatter diffraction (Supplementary Fig. 1b). Laue diffraction measurements were performed on a Multiwire MWL 120 diffractometer using a white light Cu X-ray source generated at 20 kV and -9.5 mA.



Supplementary Figure 1: (a) Optical image of MnTe₂ single crystal on mm-grid paper.(b) Representative backscattering Laue diffraction pattern along the 1 0 0 direction indicating single crystallinity.

2 Magnetic Measurements

Magnetic susceptibility measurements were obtained using a Quantum Design MPMS3 superconducting quantum interference device (SQUID). Ground crystals were added to an inverted gelatin capsule that was affixed together by Kapton tape. The gelatin capsule was then inserted into a straw and positioned for measurement. Temperature dependent magnetic susceptibility (χ vs. T) was collected upon warming from 2 K (Supplementary Fig. 2a); zero-field cooled data acquisition was done first using a 500 Oe measurement field and then field cooled data acquisition followed by cooling and measuring with the same 500 Oe field. Magnetization vs. Field (M vs. H) measurements were performed at 2 K after zero field cooling before the field was swept from 0 to $\pm 4T$ and which trace was run twice (Supplementary Fig. 2b).



Supplementary Figure 2: (a) Measurement of single crystal magnetic susceptibility vs. temperature with a 1 T applied field along [1 0 0]. (b) Measurement of magnetization v.s. field below and above the magnetic transition.

3 Linear Spin Wave Theory

The crystal structure of MnTe₂ belongs to the space group $Pa\bar{3}$ (205) which has four Mn sublattices at the WP 4a:

$$\begin{aligned}
 r_A &= (0, 0, 0) \\
 r_B &= (a/2, 0, a/2) \\
 r_C &= (0, a/2, a/2) \\
 r_D &= (a/2, a/2, 0)
 \end{aligned} \tag{S.1}$$

where Cartesian coordinates are used and a is the (cubic) lattice constant. In the magnetic phase below $T_N \sim 87$ K, the Mn atoms become magnetized giving rise to the non-coplanar magnetic order²:

$$\begin{aligned}
 \langle \mathbf{S}_A \rangle &\propto (+1, +1, +1) \\
 \langle \mathbf{S}_B \rangle &\propto (-1, -1, +1) \\
 \langle \mathbf{S}_C \rangle &\propto (-1, +1, -1) \\
 \langle \mathbf{S}_D \rangle &\propto (+1, -1, -1).
 \end{aligned} \tag{S.2}$$

We build our spin model based on the interaction bonds defined between pairs of sites as following:

$$\begin{aligned}
\mathbf{J}_1 : r_B &\iff r_B + (a/2, 0, -a/2) \\
\mathbf{J}_2 : r_A &\iff r_A + (a, 0, 0) \\
\mathbf{J}_3^1 : r_B &\iff r_B + (a/2, -a, -a/2) \\
\mathbf{J}_3^2 : r_B &\iff r_B + (a/2, 1, -a/2) \\
\mathbf{J}_4^1 : r_A &\iff r_A + (a, 0, -a) \\
\mathbf{J}_4^2 : r_A &\iff r_A + (a, a, 0) \\
\mathbf{J}_5^1 : r_B &\iff r_B + (a/2, 0, -3a/2) \\
\mathbf{J}_5^2 : r_B &\iff r_B + (3a/2, 0, -a/2)
\end{aligned} \tag{S.3}$$

where \mathbf{J}_2 , \mathbf{J}_4^1 and \mathbf{J}_4^2 are constrained by inversion $\{-1|0\}$ and therefore take the general symmetric form:

$$\mathbf{J}_{i=2,4} = \begin{pmatrix} J_i^{xx} & \Gamma_i^{xy} & \Gamma_i^{xz} \\ \Gamma_i^{xy} & J_i^{yy} & \Gamma_i^{yz} \\ \Gamma_i^{xz} & \Gamma_i^{yz} & J_i^{zz} \end{pmatrix} \tag{S.4}$$

and the rest of bonds are not symmetry-constrained, so therefore take the general form:

$$\mathbf{J}_{i \neq 2,4} = \begin{pmatrix} J_i^{xx} & D_i^z + \Gamma_i^{xy} & -D_i^y + \Gamma_i^{xz} \\ -D_i^z + \Gamma_i^{xy} & J_i^{yy} & D_i^x + \Gamma_i^{yz} \\ D_i^y + \Gamma_i^{xz} & -D_i^x + \Gamma_i^{yz} & J_i^{zz} \end{pmatrix} \tag{S.5}$$

We calculate the magnon band structure using the equation of motion (EOM) approach³ in which the low-energy dynamics is captured by the small deviations of spins from their ordered directions :

$$\mathbf{s}_i \equiv \mathbf{S}_i - \langle \mathbf{S}_i \rangle \Rightarrow \mathbf{s}_i = (s_i^x, s_i^y, 0) \tag{S.6}$$

where (S^x, S^y) are the transverse spin components in its local frame that is locally rotated such that the z-axis is aligned along the polarization direction $\langle \mathbf{S}_i \rangle = S_i \hat{z}_i = (0, 0, S_i)$, and $|s_i| \ll S_i$. By expanding the Hamiltonian in terms of the deviations, then considering their Heisenberg EOM, we reach a dynamical EOM that governs the spinwave dynamics:

$$-i \frac{ds_i^\alpha}{dt} = \sum_{j,\beta} (\mathbf{M} \cdot \mathbf{R})_{i\alpha,j\beta} s_j^\beta \tag{S.7}$$

where $\mathbf{M}_{i\alpha,j\beta} = \delta_{i,j} (\sigma_y)^{\alpha,\beta}$ with σ_y is y-Pauli matrix and \mathbf{R} is a $2N \times 2N$, where N is the number of spins in the primitive magnetic unit cell, is a semi-positive definite hermitian matrix that describes the spin-spin interactions and is referred to as the ‘‘magnon’’ Hamiltonian. The spectrum is then calculated as the eigenvalues of $\mathbf{M} \cdot \mathbf{R}$. Using the constructed spin model in Table 1, we obtain the magnon Hamiltonian $\mathbf{R}(\mathbf{k})$, diagonalize $\mathbf{M} \cdot \mathbf{R}(\mathbf{k})$ and find the magnon spectrum as shown in Fig. 2 and the magnon wavefunctions which are used to calculate the *irreps* of magnon bands at the high-symmetry momenta.

To directly compare with the experimental data, as shown in Supplementary Figs. 3 4 5 6, we compute the neutron scattering cross section, which is given by

$$\frac{d^2\sigma}{d\Omega dE} \propto \sum_{\alpha\beta} \left(\delta_{\alpha\beta} - \frac{Q_\alpha Q_\beta}{Q^2} \right) S^{\alpha\beta}(\mathbf{Q}, E), \tag{S.8}$$

where $\alpha, \beta = x, y, z$ denote cartesian components, Q_α is the α -component of the momentum transfer \mathbf{Q} , and $S^{\alpha\beta}(\mathbf{Q}, E)$ is the dynamical spin-spin correlation function.

The latter is defined as

$$S^{\alpha\beta}(\mathbf{Q}, E) = \frac{1}{N} \sum_{ij} e^{i\mathbf{Q} \cdot (\mathbf{r}_i - \mathbf{r}_j)} \int_{-\infty}^{\infty} \langle S_i^\alpha S_j^\beta(t) \rangle e^{-iEt} dt, \tag{S.9}$$

where N is the total number of spins, \mathbf{r}_i denotes the position of site i , and S_i^α is the α -component of the effective spin operator S_i .

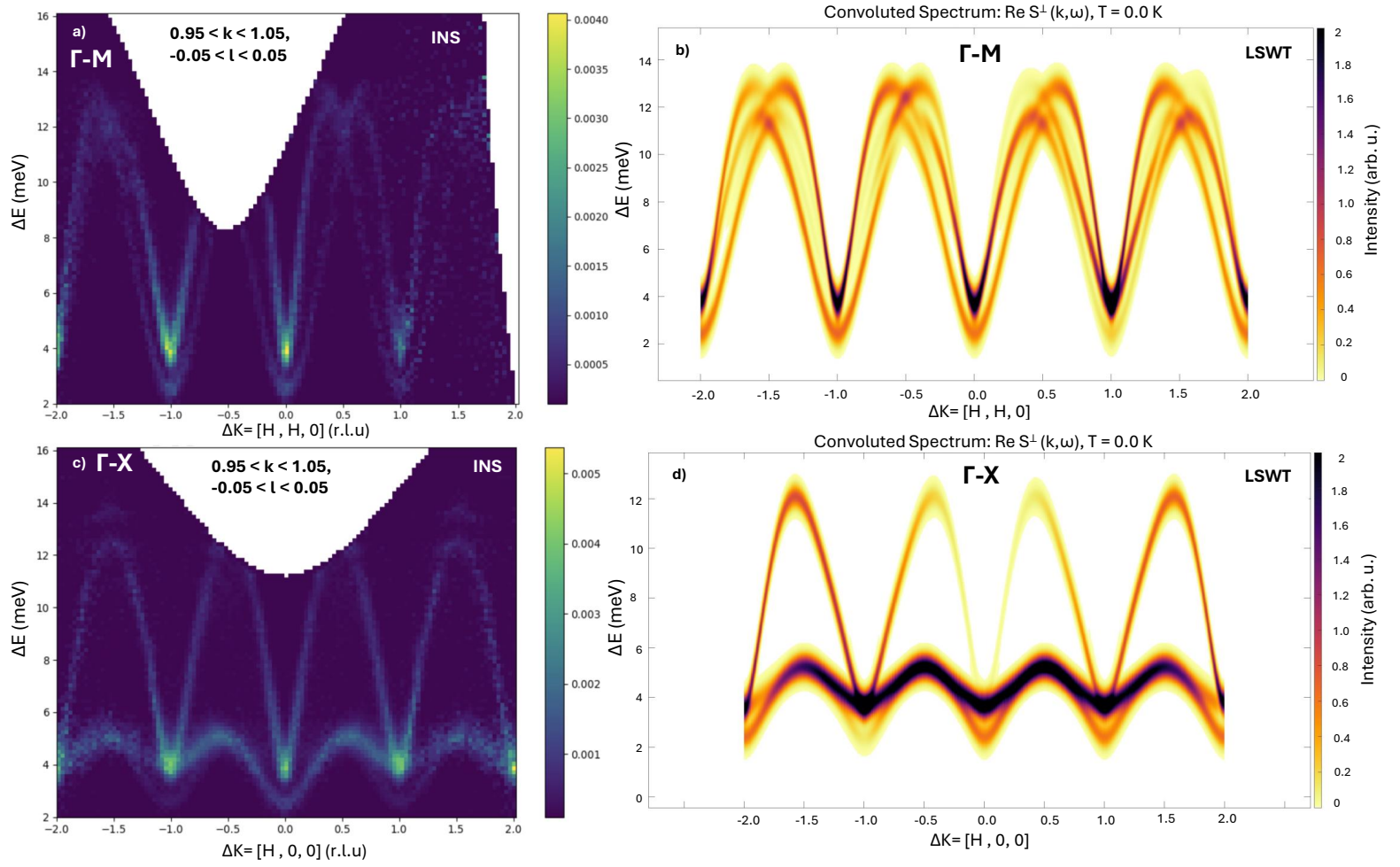
4 Magnon Nodal Lines

The enforcement of the magnon nodal loops can be explained from the connectivity of the magnon *irreps* as following. Starting from the point $X(0, \pi, 0)$ we have $X_1(2)$ and $X_2(2)$ *irreps* which decompose as following when moving from $X(0, \pi, 0)$ to $DT(0, v, 0)$:

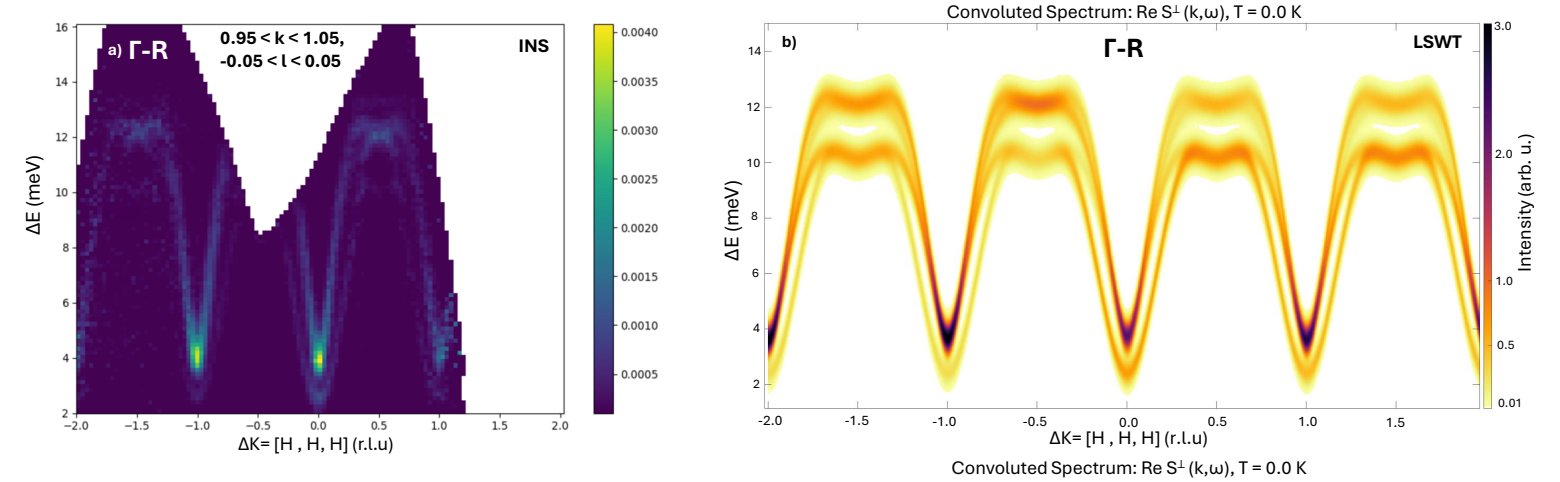
$$\begin{aligned}
X_1(2) &\rightarrow DT_2(1) \oplus DT_3(1) \\
X_2(2) &\rightarrow DT_1(1) \oplus DT_4(1)
\end{aligned}$$

and as going from $DT(0, v, 0)$ to $A(u, v, 0)$:

$$\begin{aligned}
DT_1(1) &\rightarrow A_1(1) \\
DT_2(1) &\rightarrow A_2(1) \\
DT_3(1) &\rightarrow A_2(1) \\
DT_4(1) &\rightarrow A_1(1)
\end{aligned}$$



Supplementary Figure 3: Experimental and simulated INS intensity on the $\Gamma - M$ and $\Gamma - X$ cuts. a) Experimental INS intensity on the $\Gamma - M$ line with k, l taking the highlighted values. b) Simulated INS intensity on the $\Gamma - M$ line using the spin model described in the main text. c) Experimental INS intensity on the $\Gamma - X$ line with k, l taking the highlighted values. d) Simulated INS intensity on the $\Gamma - X$ line.

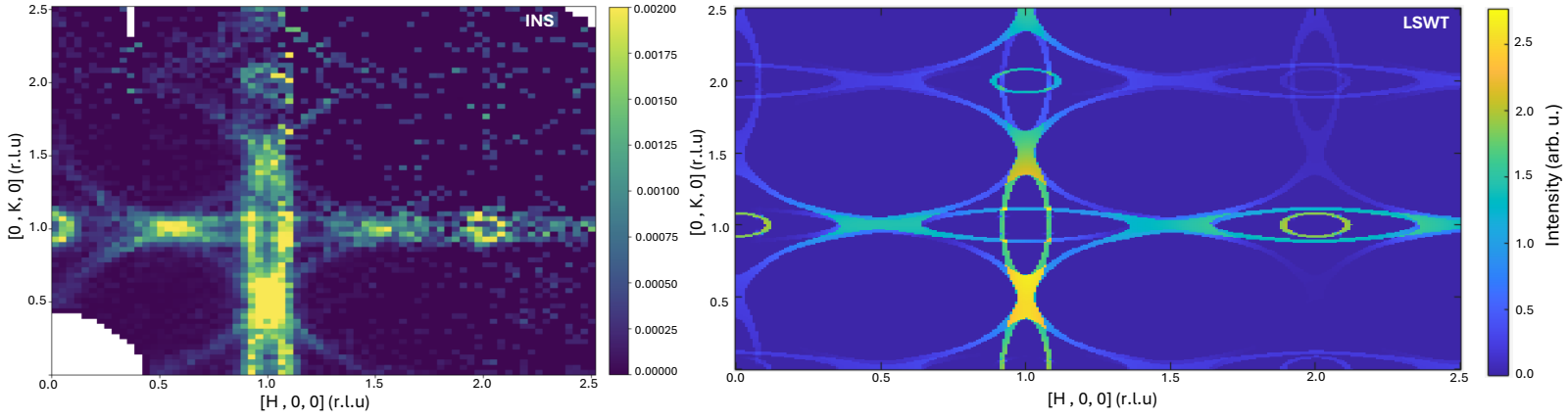


Supplementary Figure 4: Experimental and simulated INS intensity on the $\Gamma - R$ cut. a) Experimental INS intensity on the $\Gamma - R$ line with k, l taking the highlighted values. b) Simulated INS intensity on the $\Gamma - R$ line using the spin model described in the main text.

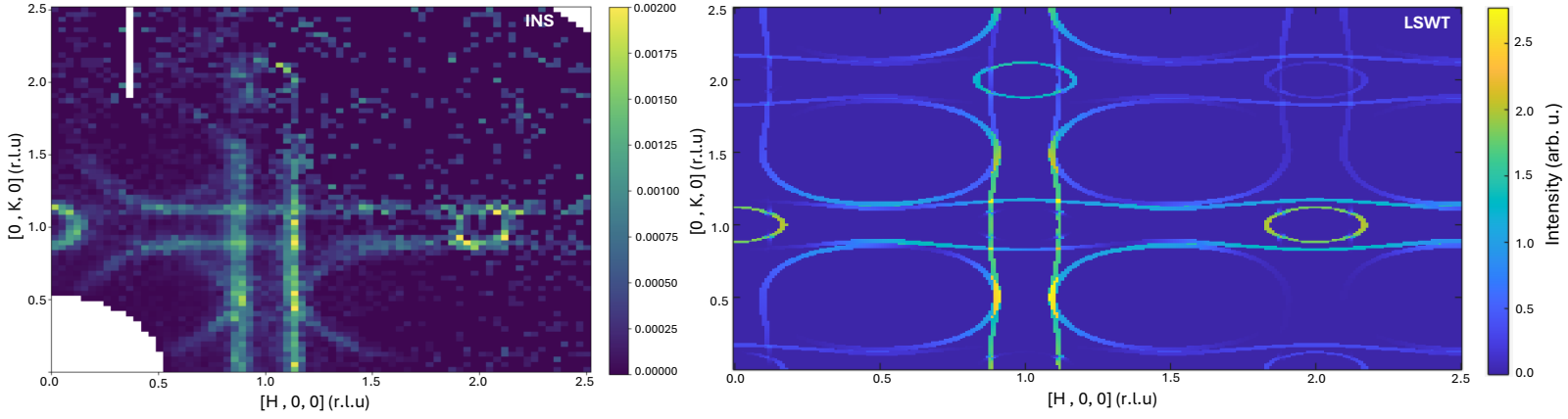
and the $A(u, v, 0)$ magnon *irreps* combine at $ZA(\pi, u, 0)$ as:

$$A_1(1) \oplus A_2(1) \rightarrow ZA_1(2)$$

which, with the correct order of *irreps* at $DT(0, v, 0)$ and $A(u, v, 0)$, results in an unavoidable crossing going from $A(u, v, 0)$ to $ZA(\pi, v, 0)$, giving rise to a nodal curve. Taking into account the symmetries of $Pa\bar{3}$, symmetry-related nodal lines exist on the $k_z = 0$ plane and in the



Supplementary Figure 5: Experimental (left) and simulated (right) INS intensity on the $k_z = 0$ plane at energy $E = 5.1$ meV within an energy window of ± 0.15 meV.



Supplementary Figure 6: Experimental (left) and simulated (right) INS intensity on the $k_z = 0$ plane at energy $E = 6.3$ meV within an energy window of ± 0.15 meV.

other $k_i = 0$ planes. The nodal lines on the different $k_i = 0$ planes and their momentum-energy structure are shown in Fig. 4 in the main text.

5 Topology of Middle Magnon Band Gap

Firstly note that the standard axes and choice of origin for both groups are the same. Then, at $\Gamma(0, 0, 0)$, the decomposition of group representations, upon application of external perturbations and breaking of magnetic space groups, goes as following:

$$\begin{aligned}\Gamma_3^+(1) &\rightarrow \Gamma_1^+(1) \\ \Gamma_4^+(3) &\rightarrow 3\Gamma_1^+(1)\end{aligned}$$

At $R(\frac{1}{2}, \frac{1}{2}, \frac{1}{2})$, equivalent to $R(\frac{1}{2}, \frac{1}{2}, \frac{1}{2})$ in the original MSG ,

$$\begin{aligned}R_2^+(2) &\rightarrow 2R_1^+(1) \\ R_3^+(2) &\rightarrow 2R_1^+(1)\end{aligned}$$

At $T(0, \frac{1}{2}, \frac{1}{2})$, equivalent to $\{3_{111}^+ | 0\} \mathbf{k}_{M(\frac{1}{2}, \frac{1}{2}, 0)}$ in the original MSG ,

$$\begin{aligned}M_1(2) &\rightarrow T_1^+(1) \oplus T_1^-(1) \\ M_2(2) &\rightarrow T_1^+(1) \oplus T_1^-(1)\end{aligned}$$

At $U(\frac{1}{2}, 0, \frac{1}{2})$, equivalent to $\{3_{111}^- | 0\} \mathbf{k}_{M(\frac{1}{2}, \frac{1}{2}, 0)}$ in the original MSG ,

$$\begin{aligned}M_1(2) &\rightarrow U_1^+(1) \oplus U_1^-(1) \\ M_2(2) &\rightarrow U_1^+(1) \oplus U_1^-(1)\end{aligned}$$

At $V(\frac{1}{2}, \frac{1}{2}, 0)$, equivalent to $M(\frac{1}{2}, \frac{1}{2}, 0)$ in the original MSG ,

$$M_1(2) \rightarrow V_1^+(1) \oplus V_1^-(1)$$

$$M_2(2) \rightarrow V_1^+(1) \oplus V_1^-(1)$$

At $X (\frac{1}{2}, 0, 0)$, equivalent to $\{3_{111}^- | 0\} \mathbf{k}_{X(0, \frac{1}{2}, 0)}$ in the original \mathcal{MSG} ,

$$X_1(2) \rightarrow X_1^+(1) \oplus X_1^-(1)$$

$$X_2(2) \rightarrow X_1^+(1) \oplus X_1^-(1)$$

At $Y (0, \frac{1}{2}, 0)$, equivalent to $X (0, \frac{1}{2}, 0)$ in the original \mathcal{MSG} ,

$$X_1(2) \rightarrow Y_1^+(1) \oplus Y_1^-(1)$$

$$X_2(2) \rightarrow Y_1^+(1) \oplus Y_1^-(1)$$

Finally, at $Z (0, 0, \frac{1}{2})$, equivalent to $\{3_{111}^+ | 0\} \mathbf{k}_{X(0, \frac{1}{2}, 0)}$ in the original \mathcal{MSG} ,

$$X_1(2) \rightarrow Z_1^+(1) \oplus Z_1^-(1)$$

$$X_2(2) \rightarrow Z_1^+(1) \oplus Z_1^-(1)$$

Out of the 10 subgroups of $Pa\bar{3}$, only 5 have nontrivial \mathcal{SI} groups. Among those, only one subgroup $P\bar{1}$ (2.4) host type-I topological magnons. This subgroup can be realized by e.g. a magnetic field along a low-symmetry direction. This achieves the required symmetry-breaking into $P\bar{1}$ and the little-group *irreps* at the *maximal* k -points of $P\bar{3}$ decompose into *irreps* of $P\bar{1}$ as detailed in Methods. Therefore three band gaps open between the magnon bands at all high-symmetry momenta. We can then calculate the $\mathcal{SI} \mathbb{Z}_2^3 \times \mathbb{Z}_4$ of each band gap using the \mathcal{SI} formula of $P\bar{1}$:

$$\begin{aligned} z_1 &= n^{\Gamma_1^-} + n^{T_1^-} + n^{Y_1^-} + n^{Z_1^-} \pmod{2} \\ z_2 &= n^{\Gamma_1^-} + n^{U_1^-} + n^{X_1^-} + n^{Z_1^-} \pmod{2} \\ z_3 &= n^{\Gamma_1^-} + n^{V_1^-} + n^{X_1^-} + n^{Y_1^-} \pmod{2} \\ z_4 &= n^{\Gamma_1^-} + n^{R_1^-} + n^{T_1^-} + n^{U_1^-} + n^{V_1^-} + n^{X_1^-} + n^{Y_1^-} + n^{Z_1^-} \pmod{4} \end{aligned} \tag{S.10}$$

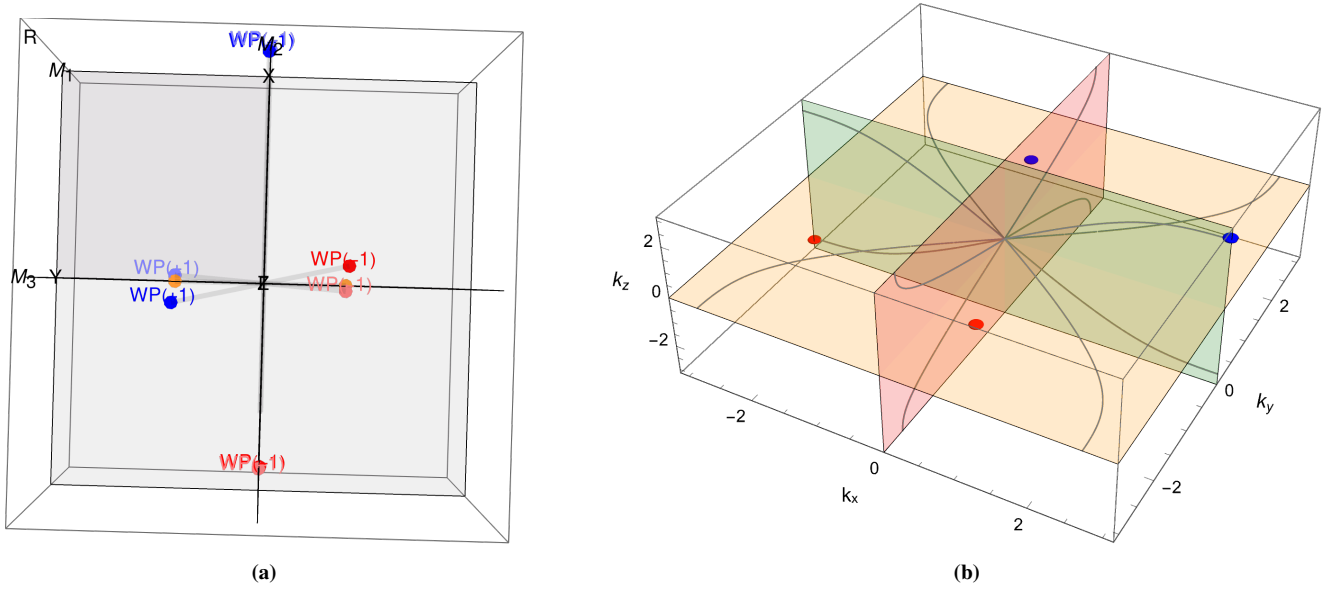
The different orders of *irreps* at the high-symmetry points result in a number of different values for each gap SI value. The possible values are summarized in Supplementary Table 1.

Supplementary Table 1: Possible values for the \mathcal{SI} in each band gap⁴ after symmetry breaking from supergroup $Pa\bar{3}$ into subgroup $P\bar{1}$. Gap i refers to the band gap between the i -th and $(i + 1)$ -th lowest energy bands. Green \mathcal{SIs} mark the realized values in a field of 14 T along the low-symmetry direction $[0\ 1\ 6]$ using the spin model obtained from fitting INS and Raman data. Findings of this paper does not depend on the details of the used low-symmetry magnetic field. The field strength of 14 T was adopted to induce a measurable middle band gap opening in future in-field INS experiments. The fourth gap refers to the collection of all four magnon bands which is always trivial. More technically, it is an elementary band representation^{4,5} induced from the local “orbitals” S_i^\pm .

Gap#	Possible \mathcal{SI} Values
1	0000, 0003, 0010, 0011, 0012 0013, 0100, 0101, 0102, 0103 0110, 0111, 0112, 0113, 1000 1001, 1002, 1003, 1010, 1011 1012, 1013, 1100, 1101, 1102 1103, 1112, 1113
2	1112
3	0000, 0001, 0010, 0011, 0012 0013, 0100, 0101, 0102, 0103 0110, 0111, 0112, 0113, 1000 1001, 1002, 1003, 1010, 1011 1012, 1013, 1100, 1101, 1102 1103, 1111, 1112
4	0000

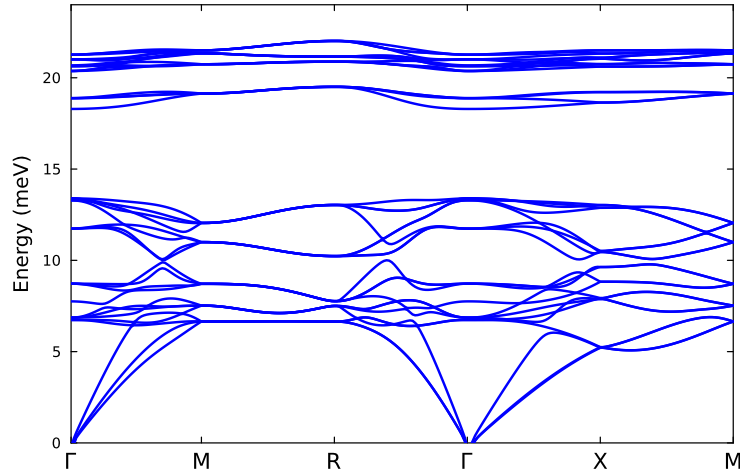
6 DFT Calculation

In order to help identify phonon modes and disambiguate them from magnon modes at similar energies, we perform density functional theory (DFT)^{6,7} calculations using the VASP code⁸⁻¹⁰ (as a check we also find very similar results with Quantum Espresso¹¹). We use a $6 \times 6 \times 6$ k -point grid, 450 eV cutoff energy, and the Mn_sv.GW and Te_GW PAW files. We perform DFT calculations using the PBEsol¹² functional and using the DFT+U framework¹³, testing U values between 1-5 eV on the Mn-3d states. U values in the range of 3-5 eV typically improve results for 3d transition metal states, which are otherwise overly delocalized due to self-interaction errors in semilocal functionals.



Supplementary Figure 7: a) Top view of the Brillouin zone showing the location of the Weyl points at different magnetic field strengths applied along $[0\ 1\ 6]$. Bold colors correspond to $B = 14$ T, light colors to $B = 5$ T, and orange to $B = 0$ T where the crossing points become part of the nodal lines, as discussed in the main text. b) Weyl points emerging after the symmetry lowering through a 9 T magnetic field along the $[0\ 1\ 6]$ direction. Weyl points are slightly off the $k_i = 0$ planes as discussed in main text. The grey lines mark the nodal lines before applying the magnetic field.

Calculations are performed using the experimental antiferromagnetic non-collinear spin structure and with spin-orbit coupling. Phonon calculations are performed in a finite difference framework using the Phonopy code^{14,15}.



Supplementary Figure 8: DFT Calculation of Phonon Dispersion. Full dispersion of phonons along high symmetry directions. In the range from 10 meV to 15 meV, there are phonons in the M-R momentum direction that overlap with magnons.

We find the best agreement overall with the experimental Raman measurements are at $U = 5$ eV with the experimental volume. However, $U = 3 - 5$ eV calculations with calculated volumes are broadly in agreement with Raman data as well. We note that these calculations do not include possible coupling between phonon and magnon modes. In Supplementary Fig. 8, we show the phonon dispersion, in order to compare with the neutron data and LSWT fit in Figs. 1-2 of the main text. Due to the 12 atoms in the primitive unit cell, there are a large number of phonon modes, many of which overlap with the energy range of the magnons. In particular, we note the phonon bands from 10 – 14 meV which can account for the extra non-magnon bands in the Fig. 2. For example, the phonon modes from M-R at 10 – 13 meV match the bands above and below the magnon bands in Fig. 2.

7 Raman Polarization and Temperature Dependence

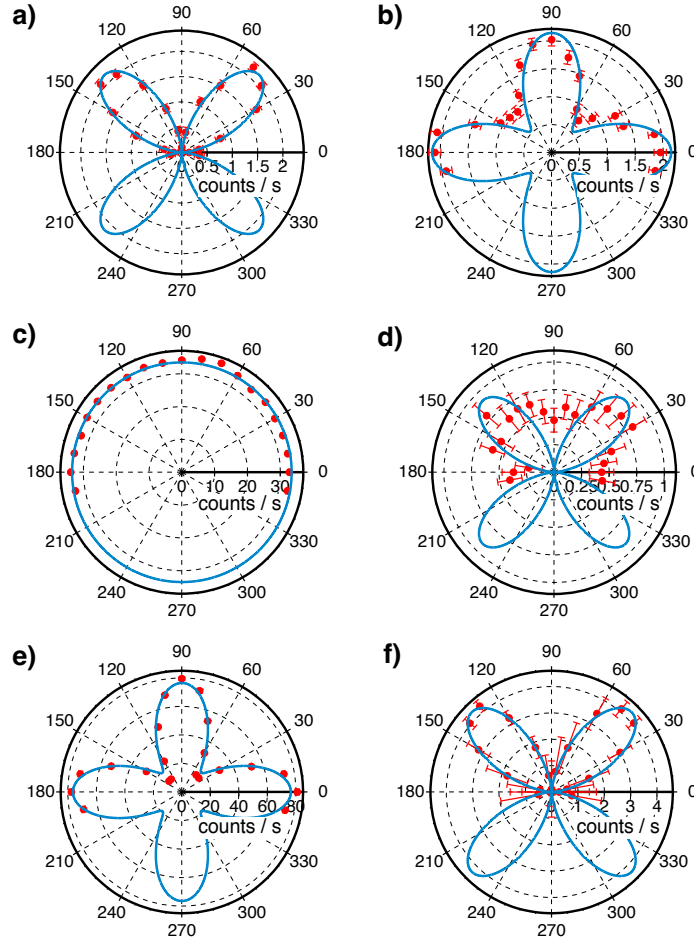
With the point group $m\bar{3}$, the Raman active modes are: A_g , E_g (note that E_g is not an irreducible representation but here we are combining two irreducible representation into a single E_g) and T_g , with the Raman tensors:

$$A_g : \begin{bmatrix} a & 0 & 0 \\ 0 & a & 0 \\ 0 & 0 & a \end{bmatrix}$$

$$E_g : \begin{bmatrix} b & 0 & 0 \\ 0 & be^{-\frac{2\pi i}{3}} & 0 \\ 0 & 0 & be^{\frac{2\pi i}{3}} \end{bmatrix} \text{ and } \begin{bmatrix} b & 0 & 0 \\ 0 & be^{\frac{2\pi i}{3}} & 0 \\ 0 & 0 & be^{-\frac{2\pi i}{3}} \end{bmatrix}$$

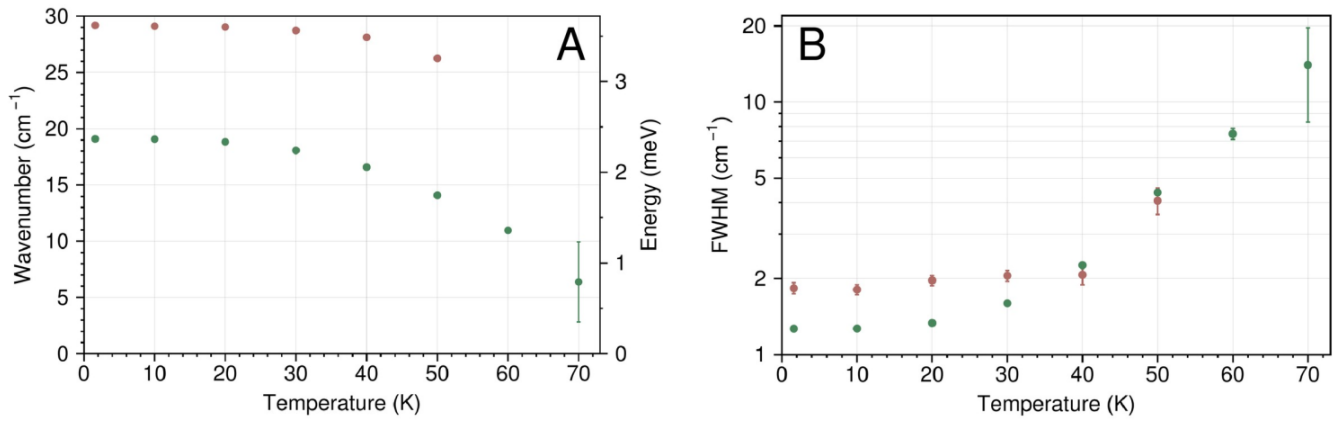
$$T_g : \begin{bmatrix} 0 & c & 0 \\ c & 0 & 0 \\ 0 & 0 & 0 \end{bmatrix}, \begin{bmatrix} 0 & 0 & c \\ 0 & 0 & 0 \\ c & 0 & 0 \end{bmatrix} \text{ and } \begin{bmatrix} 0 & 0 & 0 \\ 0 & 0 & c \\ 0 & c & 0 \end{bmatrix}$$

The theoretical response at zero external magnetic field and parallel polarizations are calculated and used to fit the experimental data. When the incoming and outgoing polarization rotate in bc plane, the Raman response for the phonons are: $A_g: a^2$, $E_g: 2b^2(\sin^4 \theta + \cos^4 \theta - \sin^2 \theta \cos^2 \theta)$, $T_g: c^2 \sin^2 2\theta$, where a , b , and c come from the Raman tensors above. The Raman response for four phonons are measured and compared to the theoretical calculations, and the symmetries are identified as, from low energy to high energy, T_g , E_g , A_g , and T_g shown in Supplementary Fig. 9 as panels (a), (b), (c), and (d), respectively. Notice that the Raman response for a T_g phonon should have nodes but there is not one in the experimental results for the highest energy phonon. This is likely due to the small scattering signal from this phonon (see Fig. 1 in the main text). The polarization response for the magnons is also shown in this figure, as panels (e) and (f), where their symmetries are identified as E_g and T_g in order of increasing energy.



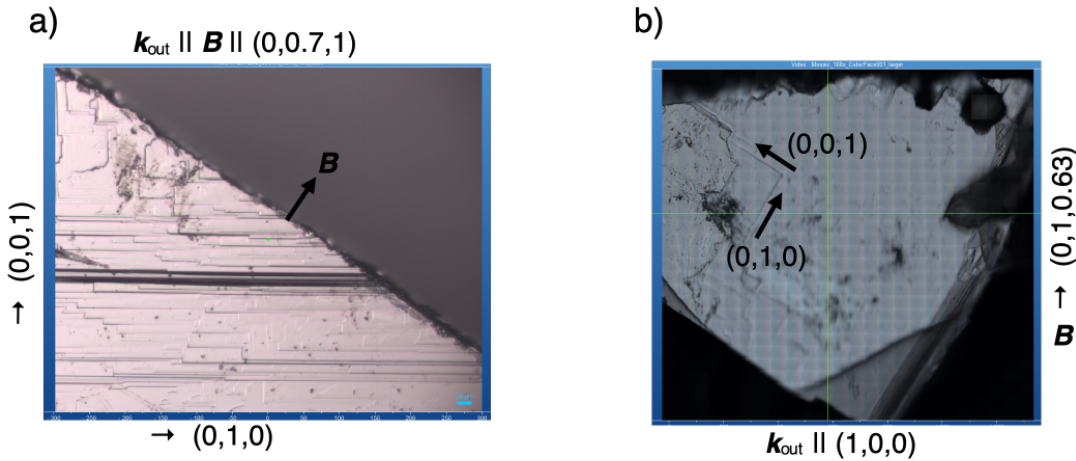
Supplementary Figure 9: Raman Polarization dependence (dots: experimental result; lines: theoretical fit) in parallel polarizers configuration of the Raman response of the phonons (a), (b), (c), and (d) in order of increasing energies, as shown in Fig. 1, and magnons (e) and (f) in Fig. 1.

The temperature dependence of the magnon energies and full width at half maxima are shown in Supplementary Fig. 10. As expected, the magnon energies soften (decrease) and their widths increase as the temperature increases toward the Neel temperature.



Supplementary Figure 10: Temperature dependence of Γ -magnons measured by Raman spectroscopy. A) Energies of magnon bands as a function of temperature. The red (green) dots denote the energy of the measured triplet (singlet) magnon. B) FWHM of the triplet and singlet magnon bands as a function of temperature. As T_N is approached, the energies of the magnon modes centers decrease and have broader bandwidths.

To figure out the direction of the magnetic field along low symmetry directions, photographs of the crystals were used to determine the cubic axes following striations of the crystal along the cubic axes (1,0,0), (0,1,0), and (0,0,1). In the Faraday configuration, where the magnetic field is applied along the direction of propagation of the outgoing photon, $k_{out} \parallel B$, a crystal was polished with a wedge under it to create a surface not perpendicular to any of the cubic axes. The direction perpendicular to this surface was determined as shown in panel a) of Supplementary Fig. 11, using simple trigonometry by inspecting the angles that the cubic directions striations make to the wedged surface. In the Voigt configuration, where the applied magnetic field is perpendicular to the direction of propagation of the outgoing photon, $k_{out} \perp B$, a crystal was rotated around the (1,0,0) axis by a small angle and the vertical direction was chosen as the direction of the magnetic field. The angles were determined similarly to the Faraday case using simple trigonometry of the striations of the crystal. This is shown in panel (b) of Supplementary Fig. 11.



Supplementary Figure 11: Determination of magnetic field direction in the two crystals used in the Raman experiments. Samples used in the Faraday a) and Voigt b) configurations experiments, with the cubic axes labeled and the magnetic field directions marked.

References

- [1] Nelson, R. A. *et al.* Axis dependent conduction polarity in the air-stable semiconductor, *pdse2*. *Mater. Horiz.* **10**, 3740–3748 (2023). URL <http://dx.doi.org/10.1039/D3MH00537B>.
- [2] Burel, P. *et al.* Noncollinear magnetic structure of mnt_2 . *Phys. Rev. B* **56**, 14013–14018 (1997). URL <https://link.aps.org/doi/10.1103/PhysRevB.56.14013>.
- [3] Lu, F. & Lu, Y.-M. Magnon band topology in spin-orbital coupled magnets: classification and application to α - $rucl_3$ (2018). URL <https://arxiv.org/abs/1807.05232>.
- [4] Karaki, M. J. *et al.* High-throughput discovery of perturbation-induced topological magnons. *npj Computational Materials* **11** (2025). URL <http://dx.doi.org/10.1038/s41524-025-01706-2>.
- [5] Karaki, M. J. *et al.* An efficient material search for room-temperature topological magnons. *Science Advances* **9**, eade7731 (2023). URL <https://www.science.org/doi/abs/10.1126/sciadv.ade7731>. <https://www.science.org/doi/pdf/10.1126/sciadv.ade7731>.
- [6] Hohenberg, P. & Kohn, W. Inhomogeneous electron gas. *Phys. Rev.* **136**, B864–B871 (1964). URL <https://link.aps.org/doi/10.1103/PhysRev.136.B864>.

- [7] Kohn, W. & Sham, L. J. Self-consistent equations including exchange and correlation effects. *Phys. Rev.* **140**, A1133–A1138 (1965). URL <https://link.aps.org/doi/10.1103/PhysRev.140.A1133>.
- [8] Kresse, G. & Furthmüller, J. Efficient iterative schemes for ab initio total-energy calculations using a plane-wave basis set. *Phys. Rev. B* **54**, 11169–11186 (1996). URL <https://link.aps.org/doi/10.1103/PhysRevB.54.11169>.
- [9] Kresse, G. & Joubert, D. From ultrasoft pseudopotentials to the projector augmented-wave method. *Phys. Rev. B* **59**, 1758–1775 (1999). URL <https://link.aps.org/doi/10.1103/PhysRevB.59.1758>.
- [10] Shishkin, M. & Kresse, G. Implementation and performance of the frequency-dependent *gw* method within the paw framework. *Phys. Rev. B* **74**, 035101 (2006). URL <https://link.aps.org/doi/10.1103/PhysRevB.74.035101>.
- [11] Giannozzi, P. *et al.* Quantum espresso: a modular and open-source software project for quantum simulations of materials. *Journal of physics: Condensed matter* **21**, 395502 (2009). URL <https://iopscience.iop.org/article/10.1088/0953-8984/21/39/395502>.
- [12] Perdew, J. P. *et al.* Restoring the density-gradient expansion for exchange in solids and surfaces. *Phys. Rev. Lett.* **100**, 136406 (2008). URL <https://link.aps.org/doi/10.1103/PhysRevLett.100.136406>.
- [13] Dudarev, S. L., Botton, G. A., Savrasov, S. Y., Humphreys, C. J. & Sutton, A. P. Electron-energy-loss spectra and the structural stability of nickel oxide: An lsd+u study. *Phys. Rev. B* **57**, 1505–1509 (1998). URL <https://link.aps.org/doi/10.1103/PhysRevB.57.1505>.
- [14] Togo, A. First-principles phonon calculations with phonopy and phono3py. *Journal of the Physical Society of Japan* **92**, 012001 (2023). URL <https://journals.jps.jp/doi/10.7566/JPSJ.92.012001>.
- [15] Togo, A., Chaput, L., Tadano, T. & Tanaka, I. Implementation strategies in phonopy and phono3py. *Journal of Physics: Condensed Matter* **35**, 353001 (2023). URL <https://iopscience.iop.org/article/10.1088/1361-648X/acd831>.